This is the author-formatted final version of Rizzi et al. (2020), Global and Planetary Change, accepted May 4th 2020, article 103210 https://doi.org/10.1016/j.gloplacha.2020.103210

Sedimentology and carbon isotope stratigraphy of the Rhaetian Hochalm section (Late Triassic, Austria)

Małgorzata Rizzi[1], Nicolas Thibault[1], Clemens V. Ullmann[1,2], Micha Ruhl[1,3,4], Troels K. Olsen[1], Julien Moreau[1], Marie-Emilie Clémence[5], Wolfgang Mette[5], Christoph Korte[1]

[1] University of Copenhagen, Department of Geosciences and Natural Resource Management, Øster Voldgade 10, 1350 København K, Denmark

[2] Camborne School of Mines, College of Engineering, Mathematics and Physical Sciences, University of Exeter, Penryn Campus, Penryn, Cornwall TR10 9FE, U.K.

[3] University of Oxford, Department of Earth Sciences, South Parks Road, Oxford OX1 3AN, U.K.

[4] Department of Geology, Trinity College Dublin, The University of Dublin, College Green, Dublin 2, Ireland.

[5] Institute of Geology, University of Innsbruck, Innrain 52, 6020 Innsbruck, Austria

Keywords: Rhaetian, sedimentology, carbon isotopes, Upper Triassic

This is the author-formatted final version of Rizzi et al. (2020), Global and Planetary Change, accepted May 4th 2020, article 103210 https://doi.org/10.1016/j.gloplacha.2020.103210

Abstract

The Rhaetian (201-209 Ma, the latest stage of the Triassic) is an important time-interval for the study of environmental changes preceding the End-Triassic Mass extinction. A detailed sedimentological and chemostratigraphic study was conducted in the lower Kössen Formation at Hochalm (Austria), the type-section of the Hochalm Member (Mb). This section exposes mid-Rhaetian sediments deposited in an intraplatform shallow marine basin on the north-western margin of the Tethys. The study highlights eight apparent shallowing-upward sequences from the middle of Unit 2 to Unit 4 of the Hochalm Mb stacked within the long-term transgression that characterizes the Kössen Formation. Both the bulk carbonate and the bulk organic matter $\delta^{13}C$ records indicate the presence of a distinct increase in carbon isotope values in the lower part of the lower Hochalm Mb. This excursion might represent a new chemostratigraphic marker that could be used for refining the Rhaetian stratigraphy and represents another important Late Triassic carbon-cycle perturbation prior to the major disturbance associated with the End Triassic biotic crisis.

This is the author-formatted final version of Rizzi et al. (2020), Global and Planetary Change, accepted May 4th 2020, article 103210 https://doi.org/10.1016/j.gloplacha.2020.103210

1. Introduction

One of the major Phanerozoic biotic crises, the End-Triassic Mass extinction (ETME), took place at the end of the Rhaetian Stage. Attention has so far focused for a large part on the ETME itself (e.g. Hallam & Wignall 1997; Pálfy *et al*., 2000; Kiessling *et al*., 2007; Ruhl et al, 2011). Some studies focused on climatic and environmental conditions at that time (e.g. Ahlberg *et al*., 2002) and ETME's precursors (e.g., Benton, 1986; Tanner *et al*., 2004) have also been conducted. The Rhaetian may, however, yield important clues to uncover the cause(s) triggering this extraordinary extinction event, including potential environmental perturbations prior to the ETME. For an improved understanding of such processes and environmental changes preceding the mass extinction, more robust chronostratigraphic frameworks across the Rhaetian Stage are needed. In Europe, Rhaetian deposits are well known from the Kössen Formation in Austria (e.g. von Buch, 1828; Suess, 1852; Urlichs, 1972; Mostler *et al*., 1978; Golebiowski, 1991), the Zu Limestone Formation in Italy (e.g. Gnaccolini, 1965; Jadoul *et al*., 1992, 2012; Lakew, 1990) and from the Csővár Formation in Hungary (e.g. Balogh, 1981; Kozur & Mock, 1991; Haas *et al*., 2010a). Comprehensive biostratigraphy and biozonation schemes based on ammonites and conodonts, have been constructed for these formations (e.g. Mostler *et al*., 1978; Krystyn, 1980, 1987; Detre *et al*., 1986; Kozur & Mock, 1991; Pálfy *et al*., 2007). The temporal resolution of these biostratigraphic schemes is however relatively low due to the longevity of index species. When coupled to biostratigraphy, carbon isotope stratigraphy has been proven to allow for high-fidelity and high-resolution global correlations throughout the Phanerozoic (e.g. Jenkyns *et al*., 2002; Jarvis *et al*., 2006; Korte & Kozur, 2010). Comprehensive high-resolution carbon isotope datasets are available for the Triassic–Jurassic transition of the Alps (e.g. Hillebrandt

et al., 2013; Morante & Hallam, 1996; McRoberts *et al*., 1997; Galli *et al*., 2005, 2007; Kürschner *et al.*, 2007; Ruhl *et al.*, 2009), the Transdanubian Range (e.g. Pálfy *et al*,. 2001, 2007; Korte & Kozur, 2011) and other European and North American successions (e.g., Hesselbo *et al*., 2002; Guex *et al*., 2004; Lindström *et al*., 2017; Ward *et al*., 2007; Williford *et al*., 2007; Korte *et al.*, 2009; Korte *et al*., 2019 and references therein). However, $\delta^{13}C$ datasets covering the Rhaetian are still sparse, are of low resolution, discontinuous and/or focus only on the upper Rhaetian (Gawlick & Böhm, 2000; Korte *et al*., 2005; Maron *et al*., 2015; Muttoni *et al*., 2014; Preto *et al*., 2013; Richoz *et al.*, 2008; Deenen et al., 2010; Whiteside & Ward, 2011; Mette *et al*., 2012; Ullmann *et al*., 2014; Zaffani *et al*., 2017, 2018). Recently, new high-resolution bulk carbonate $\delta^{13}C$ data have been documented for the upper Rhaetian of Austria (Mette et al., 2012; Korte *et al*., 2017; Mette et al., 2019). The purpose of this paper is to build an integrated chemostratigraphic framework for the Rhaetian Stage in the Eiberg Basin, Austria, by documenting high-resolution bulk carbonate and bulk organic carbon isotope variations of the mid-Rhaetian. In addition, we present detailed sedimentological data from field observations, logging and micro facies analyses for this important type section of the Hochalm Mb in the lower Kössen Formation.

2. Geological setting

The Hochalm section (47° 40' 26" N; 12° 41' 56" E) is located in the Northern Calcareous Alps (NCA), ca. 40 km southwest from Salzburg (Austria) and 3.5 km northwest of Unken village (Fig. 1). The succession is exposed along a gravel path that branches towards the east just before the final south ascent of the main trail to the top of Sonntagshorn (Fig. 2a).

This is the author-formatted final version of Rizzi et al. (2020), Global and Planetary Change, accepted May 4th 2020, article 103210 https://doi.org/10.1016/j.gloplacha.2020.103210

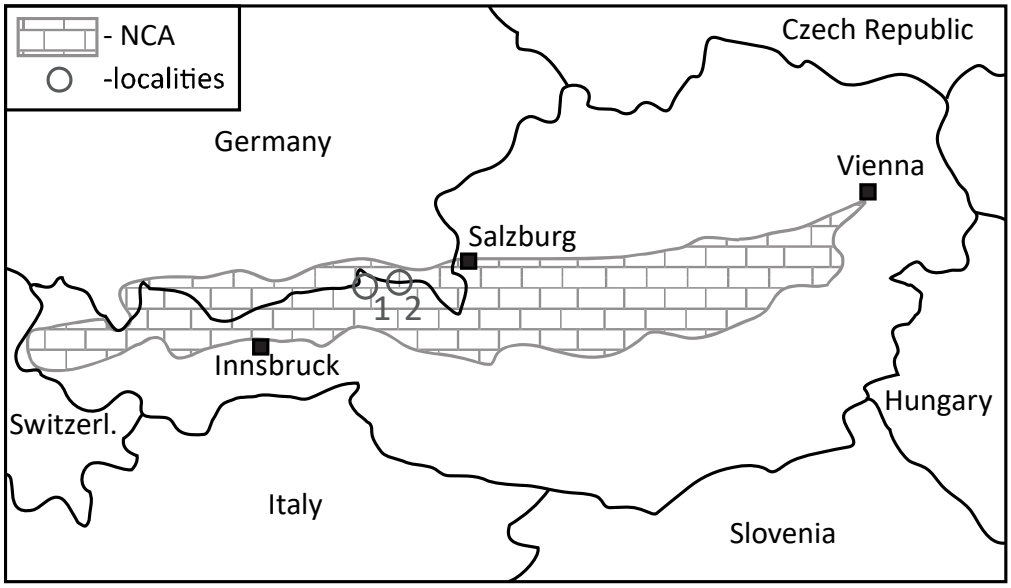

Fig. 1: Map showing the positions of the (1) Hochalm (47° 40' 26" N; 12° 41' 56" E) and (2) Eiberg (47° 33′ 00″ N, 12° 10′ 07″ E) sections. NCA: Northern Calcareous Alps.

In the Late Triassic, the northwestern margin of the Neotethys Ocean – now exposed in the Northern Calcareous Alps (NCA) – was situated in a subtropical climate belt at around 30ºN palaeolatitude (Fig. 3) (Haas *et al.*, 1995; Reinhold & Kaufmann, 2010). The shallow-water, intraplatform deposits of the studied section belong to the lower Kössen Formation (Hochalm Mb) and consist of meter-scale sequences with distinct siliciclastic-rich and carbonate-dominated interval. The sediments were deposited in a north-east, south-west oriented shallow marine intraplatform basin (Eiberg Basin) (Krystyn *et al.*, 2005) that was bordered by land in the north-west (Fig. 3a, b), and by the Dachstein reef in the south-east (Fig. 3b, c). Patch reefs (Schäfer, 1979) and fringing reefs (Bernecker, 2005) occurred locally within the basin during the deposition of the Eiberg Member. The restricted nature of the basin during Rhaetian times is not fully constrained, and it has been proposed that deep-water connections to the open ocean in the south have existed via gateways through the Dachstein reef complex (Fig. 3b) (Golebiowski, 1990; Krystyn *et al.*, 2005; Haas *et al.*, 2010b; Mette *et al.*, 2011).

This is the author-formatted final version of Rizzi et al. (2020), Global and Planetary Change, accepted May 4th 2020, article 103210 https://doi.org/10.1016/j.gloplacha.2020.103210

97

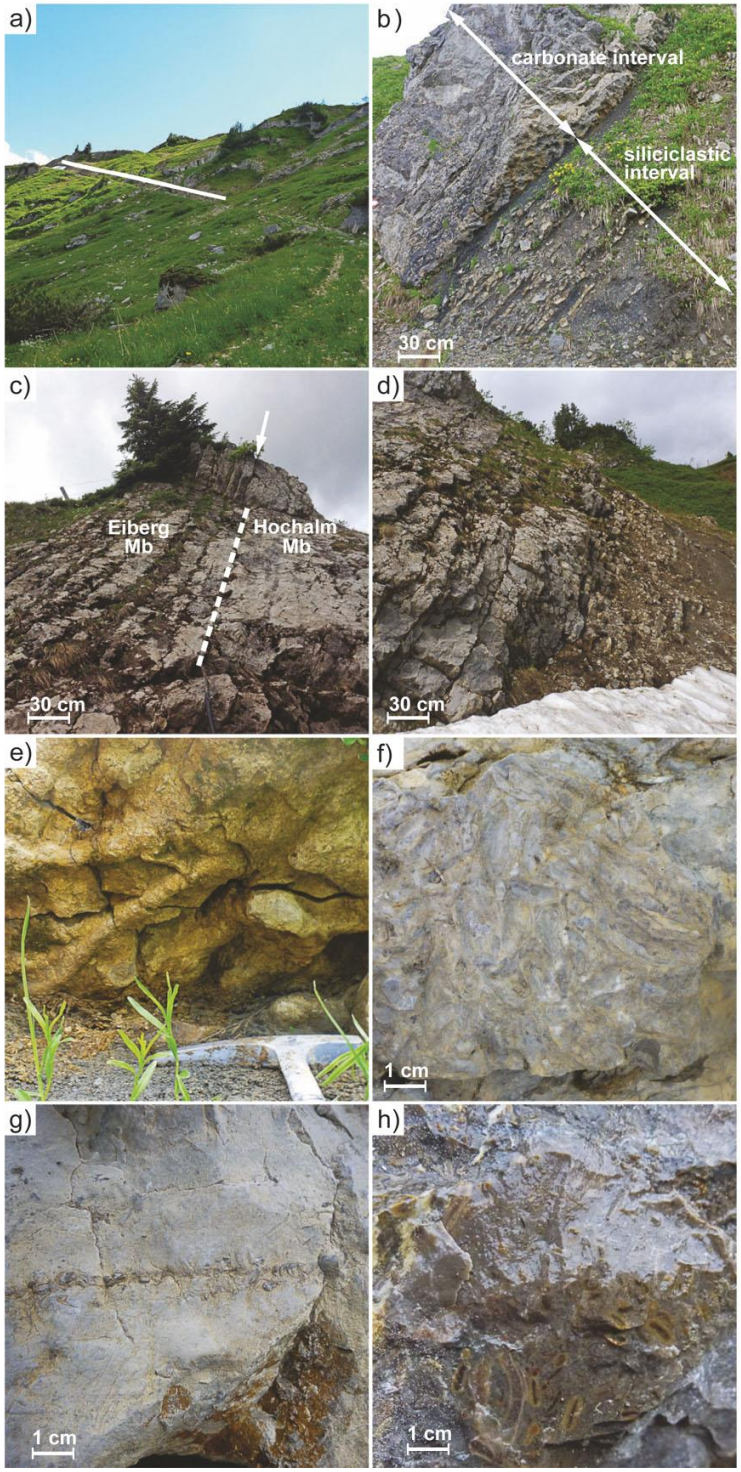

118

Fig. 2: Field photos of: **(a)** Hochalm section. The white line marks the measured profile; **(b)** section close up, where the distinct change from a siliciclastic-rich interval to a carbonate-dominated interval is visible in sequence P4; **(c)** the uppermost part of the Unit 3 and lower part of the Unit 4 (Korallenkalk) of the Hochalm Mb. Arrow points to the boundary between Hochalm and Eiberg Mb; **(d)** transition from siliclastic to carbonate interval preceding Unit 4 of the Hochalm Mb, sequence P1; **(e)** *Thalassinoides* burrows occurring at the base of carbonate interval; **(f)** Bioclastic rudstone mainly comprising

This is the author-formatted final version of Rizzi et al. (2020), Global and Planetary Change, accepted May 4th 2020, article 103210 https://doi.org/10.1016/j.gloplacha.2020.103210

119 densely packed intact and/or fragmented brachiopod and bivalve shells; **(g)** mudstone bed
120 with a layer of accumulated brachiopod shells (tempestite); **(h)** Abundant coral fragments
121 from a carbonate-rich interval. Location of the photos is marked on Fig. 5.
122 The Dachstein reef platform separated the Eiberg Basin (Austria), the Csővár Basin
123 (Hungary) and the Slovenian Trough from the outer shelf of the Tethys, though the two latter
124 basins started to form in the Carnian in the oceanward external margin of the Dachstein
125 platform and therefore, are not fully similar to the Eiberg basin. The outer shelf, known as the
126 Hallstatt Basin, constituted the transition toward the open Tethys (Mandl, 1999) and was
127 characterised by Hallstatt Facies deposits (Fig. 3c). The exact timing of the establishment of a
128 possible connection is not known, and it is unclear whether or not this gateway was open
129 during the middle Rhaetian, when the sedimentation of the here studied succession took place.
130

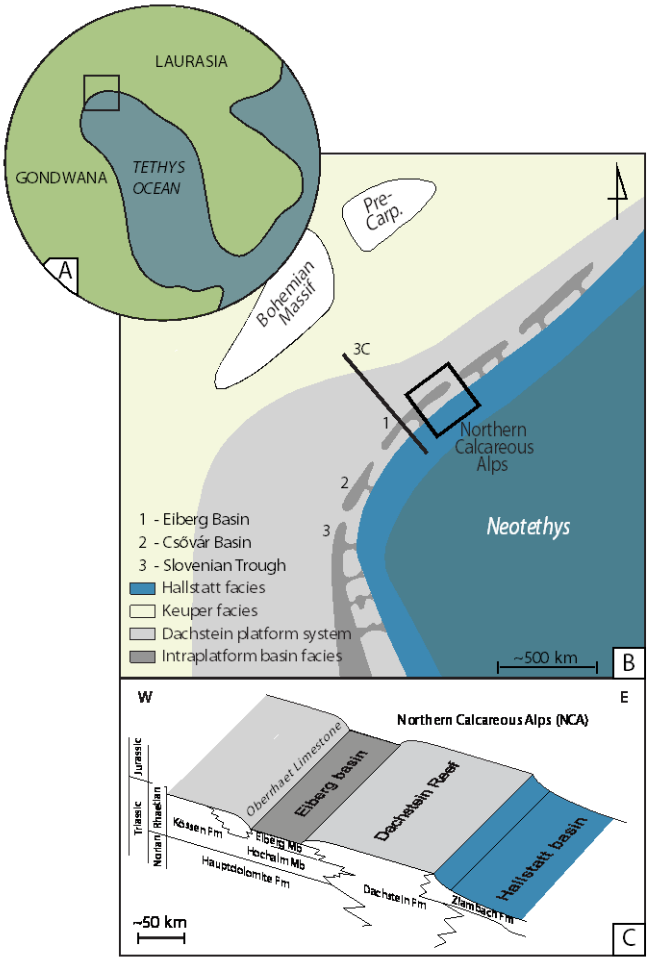

Fig. 3: Palaeogeographic maps with **(a)** simplified situation of the Tethys and **(b)** the northwest Tethyan region during the Rhaetian time. The black line indicates the position of the cross section shown in (modified after Mette *et al.*, 2019) **(c)** NW-SE cross-section of the Eiberg Basin (modified after Mette *et al.*, 2019; Haas *et al.*, 2010; Krystyn *et al.*, 2005).

3. Stratigraphic framework

3.1. Rhaetian Members and Units of the Kössen Formation

Both lithostratigraphic and biostratigraphic frameworks exist for the Hochalm section (Fig. 4). The dynamic history of the Eiberg Basin during the deposition of the Eiberg Member is well documented in the sedimentary succession and testifies to relative sea level changes which are similarly recorded in the Csővár Basin (Transdanubian Range Unit) (Haas *et al.*, 2010a), as

well as in the Lofer cycle-facies of the Dachstein platform (Fischer, 1964; Goldhammer *et al.*, 1990; Haas *et al.*, 2010b) and fringing reefs (Fig. 3c) (Schäfer, 1979). Several large-scale deepening/shallowing sequences superimposed on small-scale fluctuations related to sea level changes have been recorded (Golebiowski, 1990; Holstein, 2004) in the Hochalm Member. However, the control over the cycles remains unclear. Even in the case of the Lofer cycles there is still a discussion regarding if the cyclicity was driven by eustasy, difference in local subsidence rate or auto-cyclicity (e.g. Haas *et al.*, 2010b). Therefore, it remains unclear whether the dynamic conditions of the Eiberg basin were due to eustasy, climate change or local tectonic activity.

The Hochalm section comprises the complete Hochalm Mb and the lower part of the stratigraphically overlying Eiberg Mb (Fig. 4). Following Golebiowski (1989, 1991), the Hochalm and Eiberg Mbs are each subdivided into 4 units (Fig. 4) defined by different lithologies (Fig. 5). At Hochalm, the Hochalm Mb consists of shale/marl alternations and of coral limestone (Fig. 5), and overlies the Plattenkalk, which is supposedly of Norian age (Czurda & Nicklas, 1970).

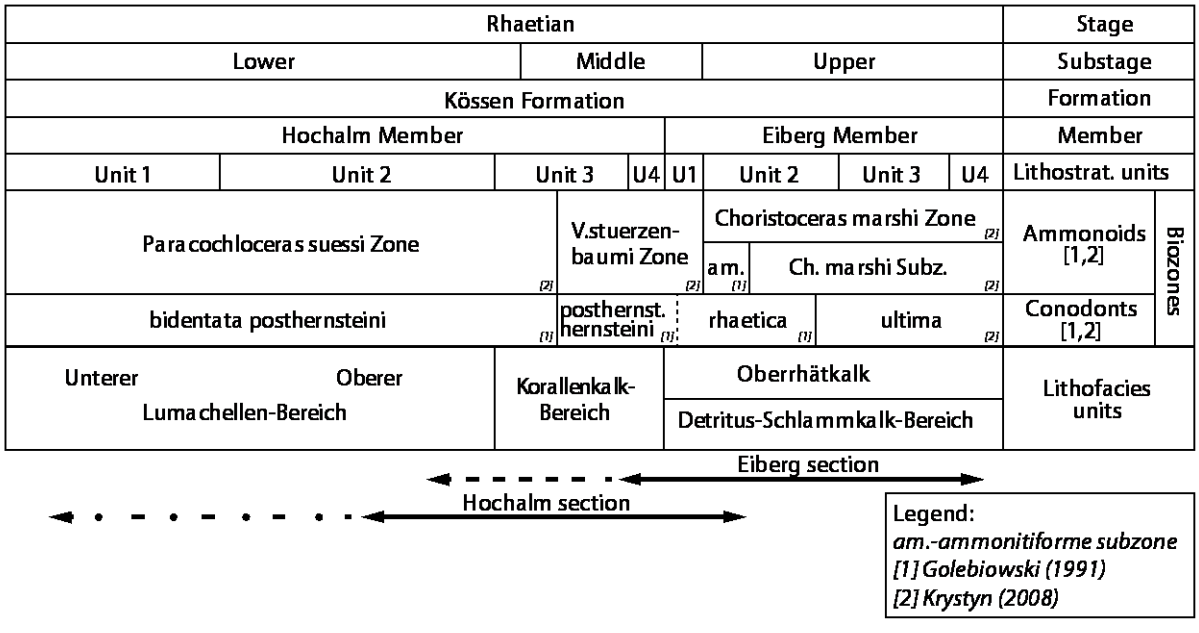

This is the author-formatted final version of Rizzi et al. (2020), Global and Planetary Change, accepted May 4th 2020, article 103210 https://doi.org/10.1016/j.gloplacha.2020.103210

Fig. 4: Stratigraphy and biozonation of the Rhaetian Hochalm and Eiberg sections (modified after Golebiowski, 1991 and Mette *et al*., 2012). Continuous arrows indicate stratigraphic extents of the two sections, while the dashed arrows indicate their nowadays covered parts but presented by Golebiowski, (1989, 1991).

The Hochalm Mb belongs biostratigraphically to the *Paracochloceras suessi* and the *Vandites stuerzenbaumi* ammonite zones (Golebiowski, 1991; Krystyn, 2008), and to the *Misikella posthernsteini* conodont zone (Kozur, 1997; Korte *et al*., 2003) (Fig. 4). For further biostratigraphic discussion, see Urlichs (1972), Mostler *et al*. (1978), Krystyn (1987, 2008, 2010), Golebiowski (1990, 1991), Kozur (1997), and references therein. The deposits of lithostratigraphic Unit 1 and the lower part of Unit 2 of Hochalm Mb are nowadays very poorly exposed at the Hochalm locality. Sampling was only possible from well-exposed marl-limestone alternations of the middle of Unit 2 of the Hochalm Mb, up to and including the lower Eiberg Mb. A 86.5-m-thick succession spanning Units 2 to 4 of the Hochalm Mb and a little more than 4 m of the lower part of Unit 1 of the Eiberg Mb have been studied in detail for sedimentology and geochemical analysis.

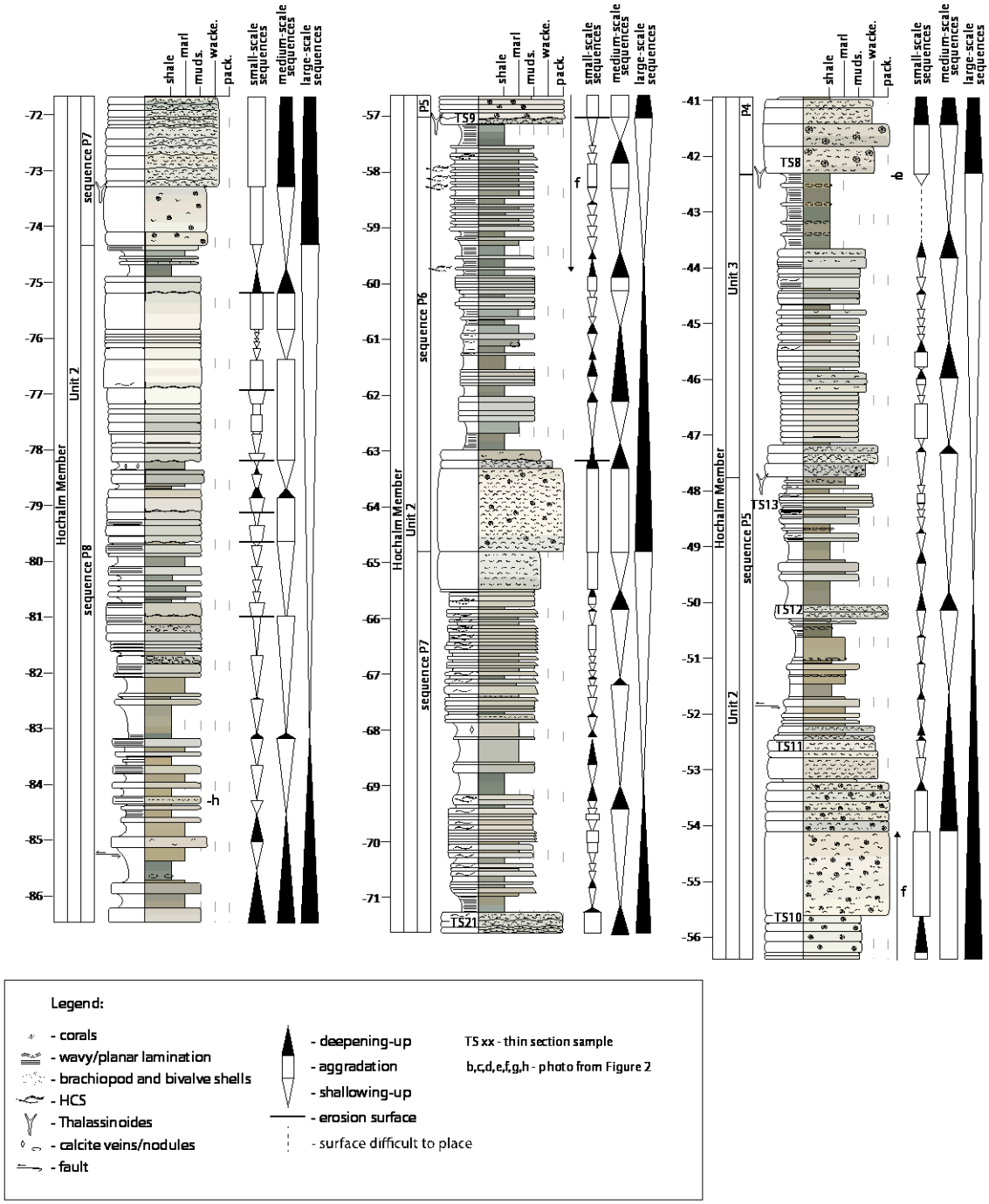

Fig. 5a: Detailed log of the Hochalm section. Colours represent true colours of the powdered sediment. Depositional sequences are marked on the right side of the profile. Eight large-scale deepening to shallowing sequences are highlighted along with sequences of lower order. Placement of the thin sections is indicated in the lithological log. Lower part of the section (-86.6 m to -41 m). For more information see text.

182

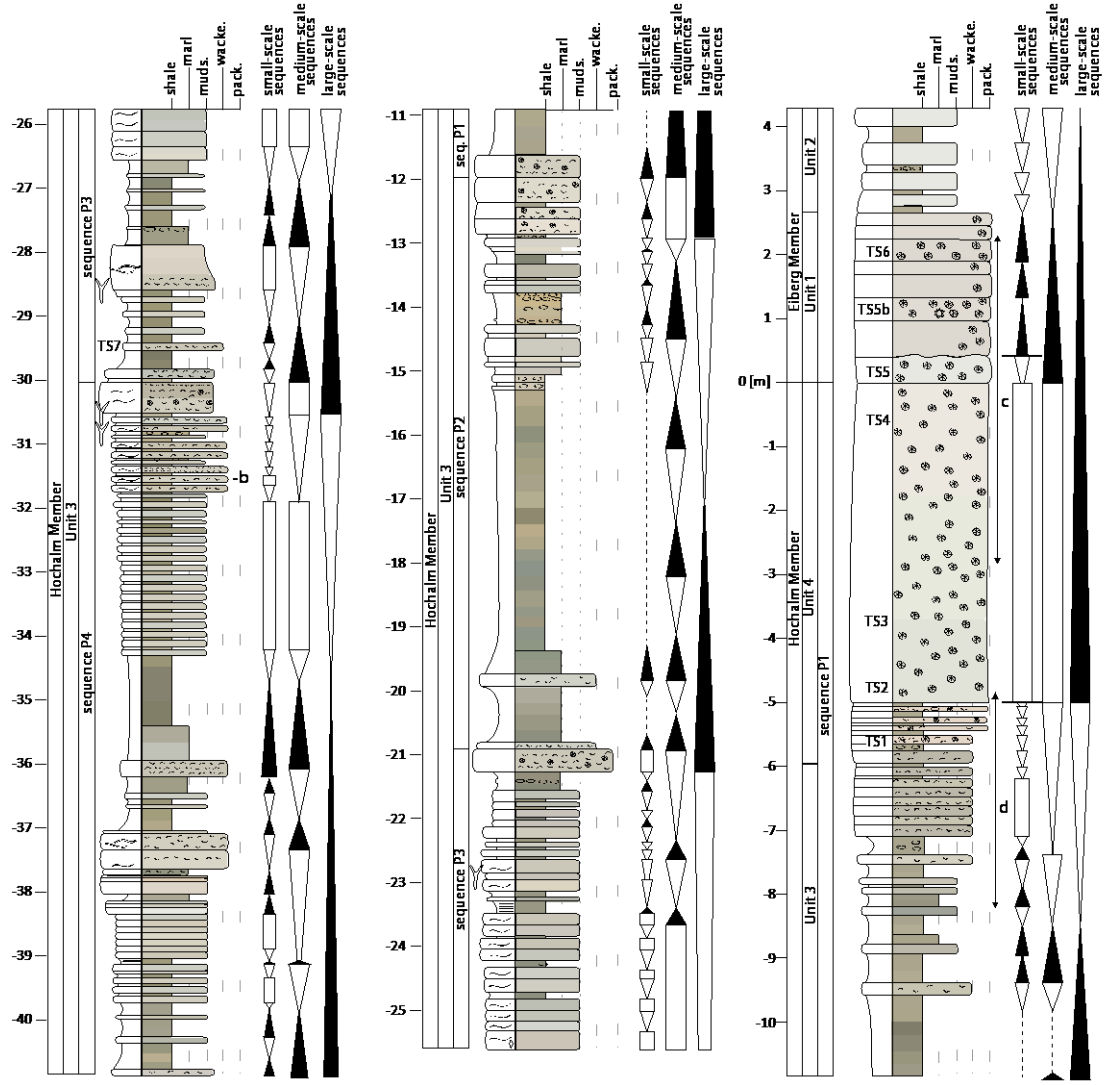

183

184 **Fig. 5b:** Continuation of Figure 5a. Upper part of the section (-41 m to +4 m).

185

186 **3.2. Facies and sequence stratigraphy of the Kössen Formation**

187 Using the comprehensive microfacies description of the Kössen Formation previously made
188 by Kuss (1983), Golebiowski (1989) resolved the lithostratigraphic sequence of microfacies
189 types and their spatial context in the studied interval. A total of 14 microfacies types were
190 classed into three distinct lithostratigraphic intervals representing distinct environmental

This is the author-formatted final version of Rizzi et al. (2020), Global and Planetary Change, accepted May 4th 2020, article 103210 https://doi.org/10.1016/j.gloplacha.2020.103210

facies associations (Fig. 6; see Appendix A): the Dachstein–lumachellite facies (Lumachellen realm, L) which essentially corresponds to a bivalve coquina facies, the Coral Limestone facies (Korallenkalk realm, K) and the Bioclastic wackestone facies (Detritus mud carbonate realm, D). Golebiowski (1991) mainly interpreted the stacking pattern of facies in the Hochalm section as shallowing-upward sequences (Fig. 7). Burgess (2001) and Tomašových (2006a) challenged this interpretation and considered that these sequences mainly reflect a combination of variations in storm frequency/intensity, and in rates of siliciclastic and carbonate supply. According to these authors, the sequences were possibly driven essentially by climatic changes (Fig. 7; Burgess, 2001; Tomašových, 2006a). In addition, Tomašových (2006a) considers that subtle facies changes within both carbonate and siliclastic dominated intervals reflect onshore-offshore gradients. Combined, all the above mentioned studies agree that deposition of the Hochalm Mb occurred in a moderately shallow marine environment. However, some discussion exists on the occurrence of potential transgressive surfaces in the overall sequence, with Golebiowski (1991) and Satterley & Brandner (1995) suggesting the existence of transgressive surfaces at the top of carbonate intervals, while Tomašových (2006a) suggests these to occur at their base (Fig. 7).

This is the author-formatted final version of Rizzi et al. (2020), Global and Planetary Change, accepted May 4th 2020, article 103210 https://doi.org/10.1016/j.gloplacha.2020.103210

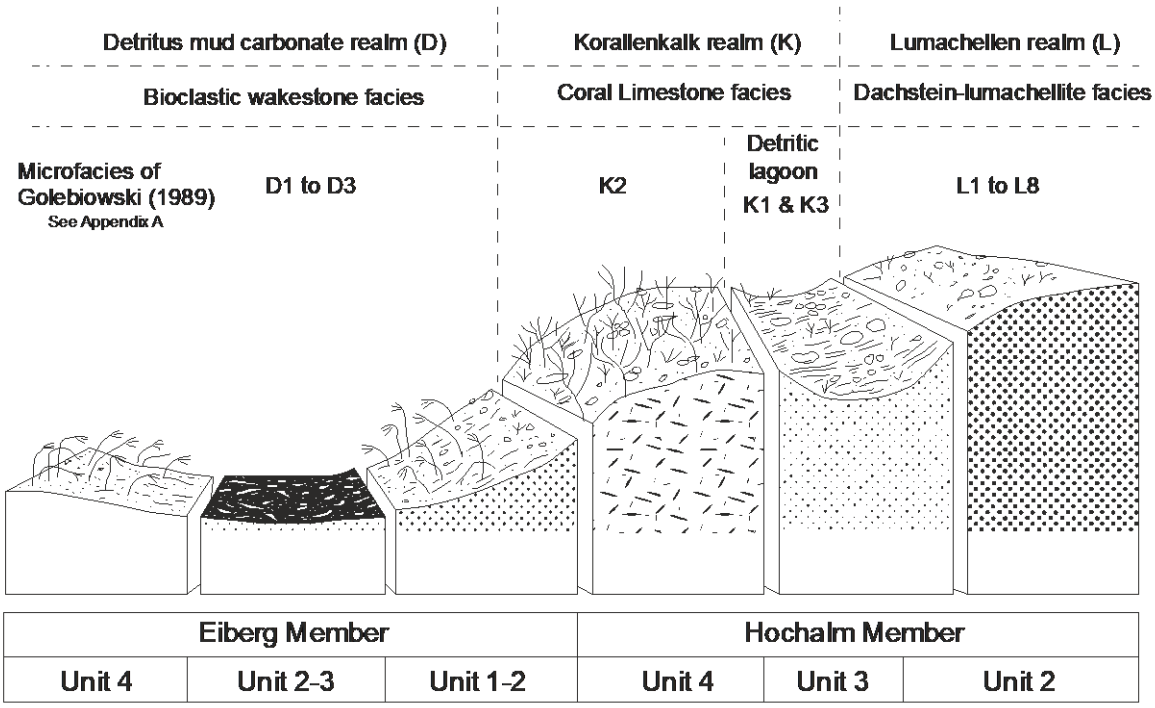

Fig. 6: Paleoenvironmental model of the Hochalm and Eiberg Mb showing the approximate extension and paleoenvironmental interpretation of the different Units (modified after Golebiowski, 1991). For more information see Appendix A.

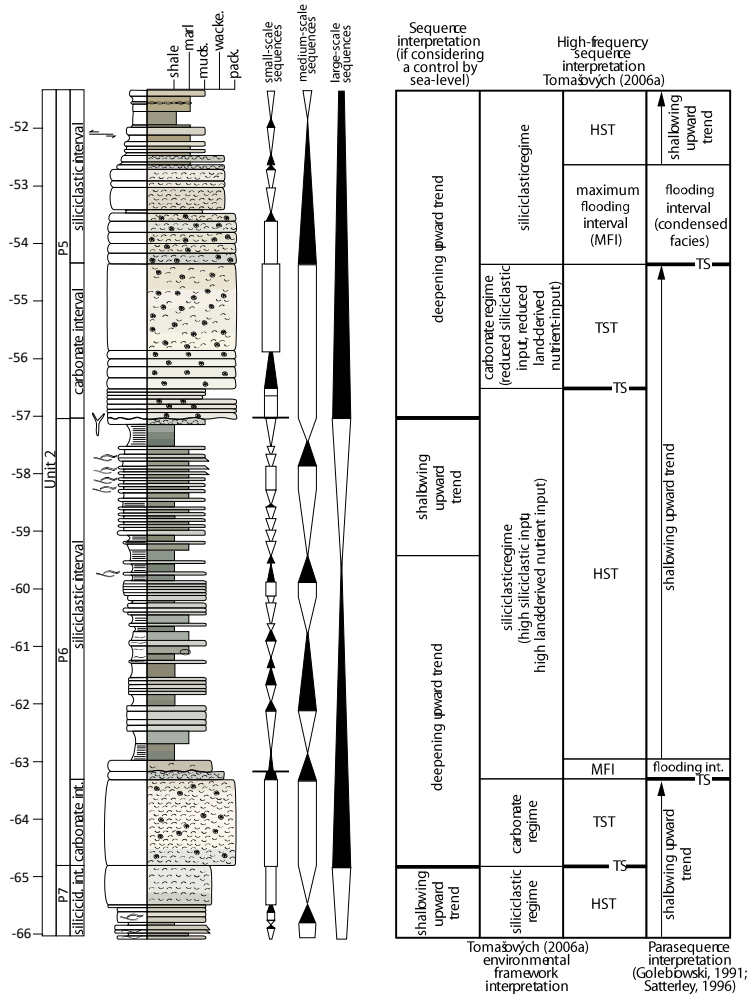

223

224 **Fig. 7:** Close up of large-scale sequence P8. On the right side of the log, the interpretation of
225 small-, medium- and large-scale sequences is presented. Different interpretations according to
226 Tomašových (2006a), Satterley (1996) and Golebiowski (1991) are shown on the right side.
227 TST: transgressive systems tract, HST: highstand systems tract, MFS: maximum flooding
228 surface, MFI: maximal flooding interval, TS: transgressive surface. For legend see Fig. 5.
229 Two hypotheses are considered for interpretation of the parasequences: either (1) they are
230 controlled by sea-level oscillations, in which case we modified the original interpretation of
231 Golebiowski (1991) of shallowing-upward and deepening-upward trends to fit better our
232 observations and standard sequence stratigraphy of carbonate sequences, either (2) they are

This is the author-formatted final version of Rizzi et al. (2020), Global and Planetary Change, accepted May 4th 2020, article 103210 https://doi.org/10.1016/j.gloplacha.2020.103210

controlled by changes in climate (humidity) that cyclically favour either a siliciclastic regime, either a carbonate regime, following the environmental interpretation of Tomašových (2006a).

4. Methods

4.1. Sample preparation

Rock samples were collected with an average spacing of 20 cm through the entire (86.5 m thick) section, and in 5 cm intervals in the lower part of sequence P5 (-54 m to -47 m, Fig. 5). A total of 244 carbonate and 418 shale and marl samples from the Hochalm Mb were processed. We did not analyse samples from the Eiberg Mb, since it is much better exposed and better preserved in the Eiberg type section (Golebiowski, 1989, 1991; Mette *et al*., 2016; Korte *et al*., 2017). Weathered surfaces were ground away and several grams of powder were generated by drilling with a tungsten carbide mill-bit from visually unaltered portions of the samples. The colour of the powdered aliquots was determined using a flatbed scanner at 200 dpi (Fig. 5).

4.2. Microfacies description

Fifteen thin sections of representative carbonate beds (Fig. 5) have been examined with a Leica DM4500P polarized-light microscope at various magnifications. The description of the microfacies followed the classification established in the area by Golebiowski (1991) (see Appendix A).

4.3. Total organic carbon (TOC) and carbonate content

For the measurement of the total organic carbon (TOC) and the estimation of $CaCO_3$ content, 193 powdered samples were weighed with a precision of ± 0.01 mg and subsequently decarbonated using 6 M HCl. After removal of acid remains via multiple steps of rinsing,

centrifugation and discarding of the supernatant, the remaining non-carbonate fraction was freeze-dried. The residual was then weighed again with the same precision as above and the $CaCO_3$ content was calculated based on the difference between sample weights before and after the decarbonation. Total organic carbon concentrations were determined on 100 mg aliquots using the Carbon Sulphur Determinator (Eltra CS 500) at the Department of Geosciences and Natural Resource Management (IGN), University of Copenhagen and recalculated for the total sample. The samples were burned in ceramic boats at ~1350°C in a catalytic oxidation process for 90 seconds. Reproducibility as measured from multiple analyses of an in-house reference material SKK-9 (TOC = 6.88%) accounts for 0.08% (1 sd, n = 31).

4.4. Bulk carbonate, calcite vein and brachiopod $\delta^{13}C$ and $\delta^{18}O$

Carbon and oxygen isotope values were obtained from the bulk carbonate (662 samples), calcite veins (3 samples) and well-preserved brachiopods (28 samples). All of the samples were analysed at the IGN, University of Copenhagen using an Iso Prime Gas Source Isotope Ratio Mass Spectrometer following the procedure described in Ullmann *et al*. (2013). Weight dependent mass fractionation was corrected using homogenized powder of Carrara Marble as an in-house standard ($\delta^{13}C$ = +1.96‰ and $\delta^{18}O$ = -1.93‰). The reproducibility of the analyses was controlled by multiple measurements of this laboratory reference material and was 0.04‰ for $\delta^{13}C$ and 0.07‰ for $\delta^{18}O$ (1 sd, n = 161).

4.5. Bulk organic carbon isotopes ($\delta^{13}C_{org}$)

Carbon isotope values of bulk organic matter were determined on the decarbonated material from 198 samples. Samples were measured using the Euro EA Elemental Analyzer coupled

with an Iso Prime Gas Source Isotope Ratio Mass Spectrometer at the IGN, University of Copenhagen. Weight dependent isotope fractionation was corrected using the in-house reference AKSil-9 ($\delta^{13}C$ = -25.65 ‰). The reproducibility of the analyses was found to be 0.3‰ for $\delta^{13}C$ (1 sd, n = 50).

5. Results

5.1. Lithology and microfacies

By convention, our 0 m level corresponds to the base of the Eiberg Member, which corresponds to the base of Unit 1 of the Eiberg Member exposed in the Eiberg quarry (Mette *et al*., 2012; Korte *et al*., 2017). Golebiowski (1989) identified a large number of long-term, 5 to 10 m thick shallowing-upward sequences in the Hochalm section composed of siliciclastic and carbonate intervals (Fig. 2b). Only eight of these sequences are documented here from Unit 2 to Unit 4 of the Hochalm Mb because most of Unit 1 and the upper half of Unit 2 were covered by soil and vegetation. The eight sequences considered in this study are defined by deepening-shallowing trends (see below) and have been numbered downward in stratigraphy in order to allow for an easy reconnection to Hochalm Mb Units 1 and 2 in the future. Five distinct lithofacies types were characterised in the field based on the combination of Folk and Dunham classifications:

(1) Massive carbonate mudstone (Fig. 2c and 2d), with cream to light grey matrix and no visible macrofossils. These beds are generally around 20 cm thick and their bases and tops are often wavy. Some of these beds are characterized by intervals with normal grain-size grading and planar to wavy laminations.

This is the author-formatted final version of Rizzi et al. (2020), Global and Planetary Change, accepted May 4th 2020, article 103210 https://doi.org/10.1016/j.gloplacha.2020.103210

(2) Bioclastic wackestone (Fig. 2e), with about 10% (estimated) shells and other bioclasts floating in a structureless cream/beige to light grey micrite. Very big, massive *Thallassinoides* burrows are often present at the base of wackestone beds.

(3) Light-coloured bioclastic rudstone (Fig. 2b), mainly comprising densely packed intact and/or fragmented brachiopod and bivalve shells. Detritus of crinoids and other echinoderms occur in lower amounts. Massive *Thallassinoides* burrows are often present at the base of individual beds.

(4) Grey-brown marls (Fig. 2b). Fossils are scarce or absent.

(5) Dark grey shales with common planar lamination (Fig. 2b). Fossils are either scarce or absent. Some of these shales are silty but a majority is fine-grained.

Within limestone lithofacies 1 and 2, thin layers of well-sorted reworked shells occur occasionally (Fig. 2g). Bioclastic wackestone (lithofacies 2) and rudstone macrofacies (macrofacies 3) are sometimes characterised by a high amount of coral debris (Fig. 2h).

The limestone lithofacies 1–3 are characterised by a large variety of distinct microfacies as discussed below (Table 1). Progressing upward in the succession, an overall increase in the siliciclastic fraction occurs from the base of the section in sequence P8 to the lower part of sequence P1 (top of Hochalm Mb Unit 3). This trend is interrupted by the occurrence of a thick coral pack-/rudstone interval (Hochalm Mb Unit 4). From among the 14 distinct microfacies defined by Golebiowski (1989) in the Kössen Fm. (Appendix A), seven were recognized in our studied samples (Table 1, Figs. 8–10). No clear systematic difference could be noted in the microfacies encountered within the beds of the siliciclastic versus carbonate intervals. According to Golebiowski (1989), carbonate microfacies of the Hochalm Mb are restricted to the Lumachellen (L) and Korallenkalk realms (K) and this is in agreement with our own observations (Table 1, Figs 8–10). Two samples at the base of Unit 1 of the Eiberg

This is the author-formatted final version of Rizzi et al. (2020), Global and Planetary Change, accepted May 4th 2020, article 103210 https://doi.org/10.1016/j.gloplacha.2020.103210

Mb show microfacies with a preponderant presence of echinoderms and fit the D1 microfacies type characteristic of the "detritus mud" carbonate facies association (Table 1, Fig. 6).

This is the author-formatted final version of Rizzi et al. (2020), Global and Planetary Change, accepted May 4th 2020, article 103210 https://doi.org/10.1016/j.gloplacha.2020.103210

Thin section label	Depth [m]	Macrofacies	Matrix	Grains	Amount	Golebiowski (1989) classification	Figures	Additional informations
TS 21	–71.55	bioclastic pack–/ grainstone	M, S	bivalve brachiopod gastropod echinoderm coral peloid	+++ ++ ++ + + +	L7a	Fig.8a,b Fig.10d	-thin horizons with horizontal alignment of the grains -some intervals are laminated -coated grains and pellets
TS 10	–55.86	mudstone	M, S	quartz	+	L6a	Fig.8c	-numerous sparite veins and stylolites
TS 11	–52.65	mud–/ wackestone	M, S	corals microsparite	+ +	K2	Fig.8d	-numerous sparite veins
TS 12	–50.30	bioclastic pack–/ grainstone	M	bivalve gastropod involutinid foraminifera peloid microsparite	+++ ++ ++ ++ +	L3	Fig.8e,f	-some bivalve shells show a dark micritic outline and geopetal sparite -some prismatic and foliated structures are preserved
TS 13	–44.70	bioclastic packstone	M	bivalve other	+++ +++	L3	Fig.8g	-some prismatic and foliated structures are preserved
TS 8	–42.05	bioclastic wackestone	M	bivalve gastropods microsparite	++ + +	K1		
TS 7	–29.45	floatstone	M	brachiopod involutinid foraminifera microsparite	+++ + +	L7b	Fig.3g Fig.8h Fig.10c	-brachiopod shells - recrystallized in sparite or filled with micritic matrix -preferential orientation of the
TS 1a	–5.60	bioclastic wacke–/ floatstone	M, S	coral bivalve	++ +	K2	Fig.9a Fig.10a	-pyrite -organic matter
TS 2	–4.75	bioclastic wackestone	M, S	coral echinoderm bivalve	+ ++ +	K1	Fig.9b	-numerous large remains of bivalve shells with foliated structure
TS 3	–3.75	bioclastic wacke–/ packstone	M, S	coral echinoderm gastropod bivalve sparite	++ ++ ++ ++ ++	K 1	Fig.9c	-poorly sorted bioclasts -organic matter, pyrite -arenitic detritus -some foliated and prismatic structure preserved in bivalves
TS 4	–0.65	bioclastic packstone	M, S	echinoderm coral bivalve	++ ++ ++	K 1	Fig.9d	-poorly sorted -mainly sparitic ghosts of bioclasts -bivalves with prismatic and foliated
TS 5	0.15	bioclastic packstone	M	bivalve echinoderm	+ +++	D 1	Fig.9e	-mainly poorly sorted sparitic ghosts of bioclasts
TS 5b	1.00	bioclastic packstone	M, S	gastropod brachiopod bivalve echinoderm microsparite	+ + + +++ ++	D 1	Fig.9f	-mainly sparitic ghosts of bioclasts
TS 6	2.10	bioclastic micropackstone	M	bivalve echinoderm gastropod brachiopod peloids lithoclasts	++ ++ + + + +	L 7b	Fig.10b Fig.9g,h	-some intervals are laminated with clear preferential horizontal orientation of the elongated bioclasts -remains of bivalve shells

Table 1: Description of the various thin sections analysed from the Hochalm section.

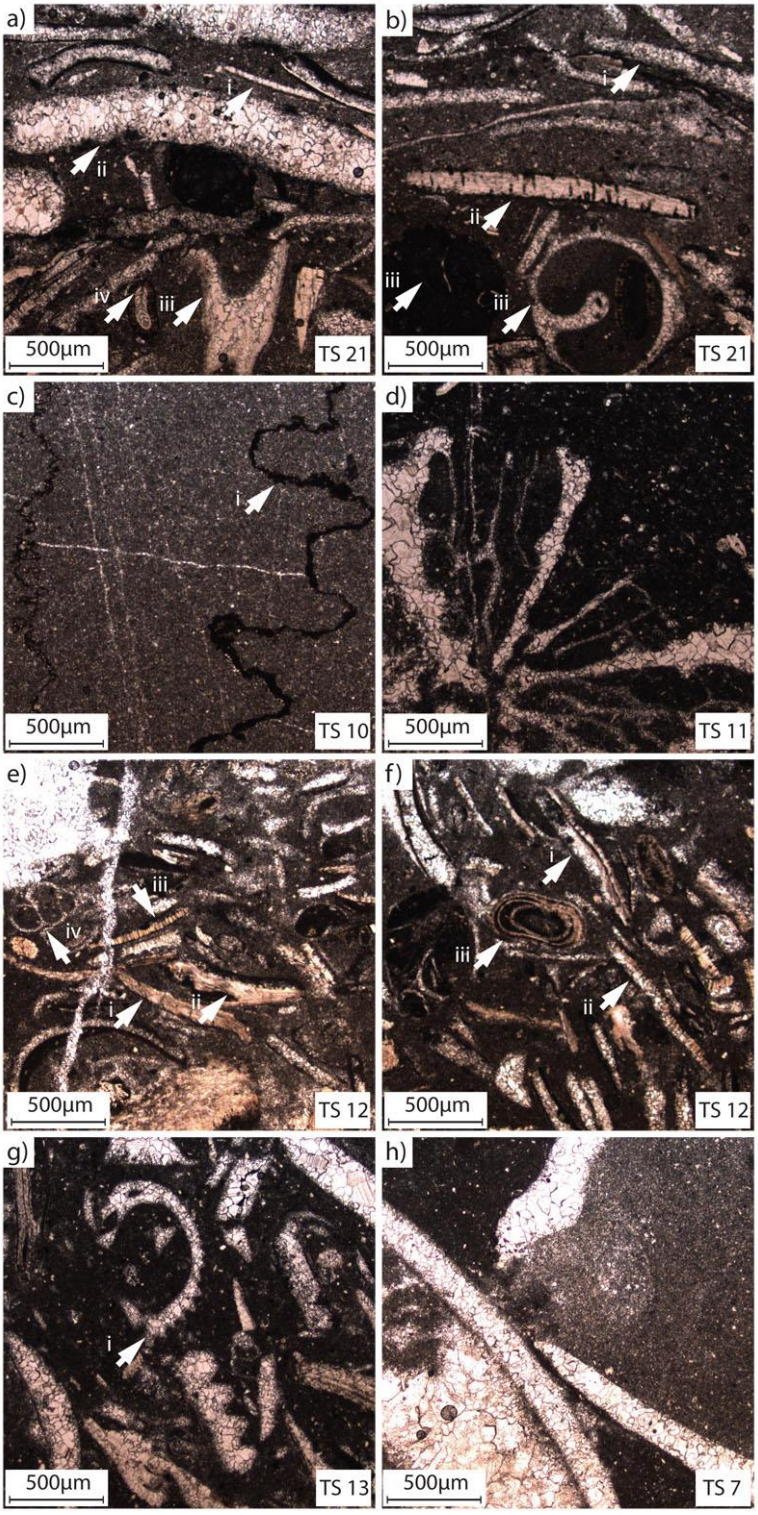

Fig. 8: Various observations of thin sections in polarized light. **a)** and **b)** sample TS21 (-71.55 m): Bioclastic packstone with a micritic matrix containing various amounts of microsparite. Some thin horizons are laminated with clasts showing a horizontal alignment (b). Most of the clasts are remains of bivalves (e.g. a i) but numerous recrystallized brachiopods (e.g. a ii) and gastropods are also present, along with few echinoderms and a number of cup-shaped corals (a iii). Facies L7a; **(c)** sample TS10 (-55.86 m): Mudstone with a matrix of micrite, very fine microsparite and terrigenous quartz grains. Numerous veins of sparite occur along with stylolytes filled with clay (c i). Facies L6a; **(d)** sample TS11 (-52.65 m): Mudstone to wackestone with a matrix of micrite and sparse microspar. Facies K2; **e)** and **f)** sample TS12 (-50.30 m): Bioclastic pack/rud-stone with a

matrix composed of micrite and sparse microspar. Most of the clasts are remains of either bivalve or brachiopod shells and many of them show a dark micritic outline and geopetal sparite (e.g. e i, ii). When preserved, the bivalve shells show a great variety of different microstructures: foliated (e.g. e i, ii), prismatic (e.g. e iii), and foliated and punctuate (b ii). Some of the shells show both, original and recrystallized structures (e.g. f i, ii).Gastropods (e iv) and small involutinid foraminifers (e.g. a iv, 9c iii, iv) are common. Peloids are common too. Facies L3; **(g)** sample TS13 (-47.70 m): Bioclastic packstone with a fine micritic matrix containing sparse microspar. Most of the clasts are remains of bivalves but brachiopods also appear (g i). A few of them have preserved foliated or prismatic microstructures. Facies L3; **(h)** sample TS7 (-29.45 m): Floatstone with a very fine micritic matrix containing sparse microspar. The clasts are entirely composed of brachiopod shells (completely recrystallized or filled with matrix). Brachiopod shells correspond to a horizontal intercalation within a mudstone bed presented in Figure 2g. Facies L7b.

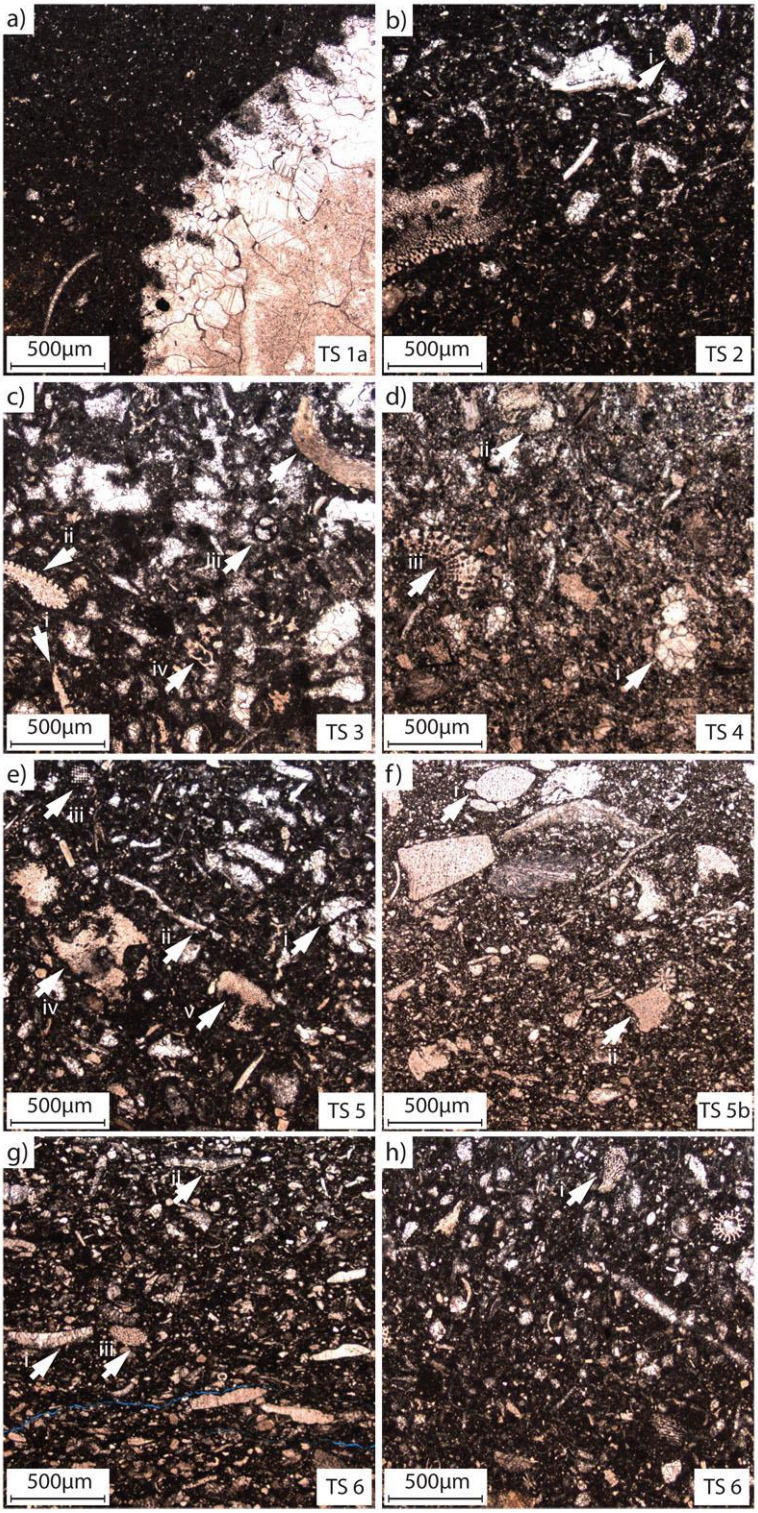

Fig. 9: Various observations of thin sections in polarized light. **(a)** sample TS1a (-5.6 m): Bioclastic wackestone/floatstone with a very fine micritic matrix with few microsparite, pyrite, and some larger coral bioclasts. Few fragments of bivalve shells. Facies K2; **(b)** sample TS2 (-4.75 m): Bioclastic wackestone with a matrix composed dominantly of fine micrite and some microsparite. The grains are debris of corals, echinoderms (b i), and bivalve shells sometimes with foliated structure. Facies K1; **(c)** sample TS3 (-3.75 m): Bioclastic wacke- to packstone with a fine- to coarse micritic matrix with few microsparitic grainsand pyrite. Diversity of poorly sorted bioclasts is high with debris of corals, bivalves (c i, with sometimes preserved foliated and prismatic structures), echinoderms (e.g. c ii, d iii) and gastropods. Large number of sub-angular sparitic clasts occurs. Facies K1**;**

This is the author-formatted final version of Rizzi et al. (2020), Global and Planetary Change, accepted May 4th 2020, article 103210 https://doi.org/10.1016/j.gloplacha.2020.103210

(d) sample TS4 (-0.65 m): Bioclastic packstone with a matrix composed of a mix of micrite and a very large amount of microsparite. The grains are mostly poorly sorted sparitic ghosts of bioclasts (d i). Debris of echinoderms (d ii, iii), corals and bivalves with prismatic and foliated structures also occurs. Facies K1**; (e)** sample TS5 (15 cm): Bioclastic packstone with sparse microspar in a micritic matrix. The grains comprise many poorly sorted sparitic ghosts of bioclasts (e i), debris of bivalves (e ii) with prismatic structure and a very high amount of echinoderms (e iii, iv, v). Facies D1**; (f)** sample TS5b (1 m): Bioclastic packstone with matrix composed of an equal amount of micrite and microsparite. The clasts comprise gastropods, many sparitic ghosts of bioclasts (f i), some of which can be identified as brachiopods, bivalves and a very high amount of echinoderms (f ii). Facies D1**; (g** and **h)** sample TS6 (2.10 m): Bioclastic fine grained packstone with a micritic matrix and sparse microspar. Some lithoclasts with a mudstone texture and rare peloids (h) are present. The bioclasts are remains of bivalves (mostly; e.g. g i, ii) and numerous echinoderms (e.g. g iii, h i), few gastropods and brachiopods are also present. The bioclasts are sorted in two main categories: roundish to angular, 50 to 100 µm long clasts and 200 to 500 µm long elongated bioclasts which are mostly remains of bivalve shells (g). Some intervals are laminated. Non-laminated intervals show no favored orientiation of the bioclasts (g) whereas a clear preferential horizontal orientation of the elongated bioclasts is observed in the laminated interval (g). Facies L7b.

This is the author-formatted final version of Rizzi et al. (2020), Global and Planetary Change, accepted May 4th 2020, article 103210 https://doi.org/10.1016/j.gloplacha.2020.103210

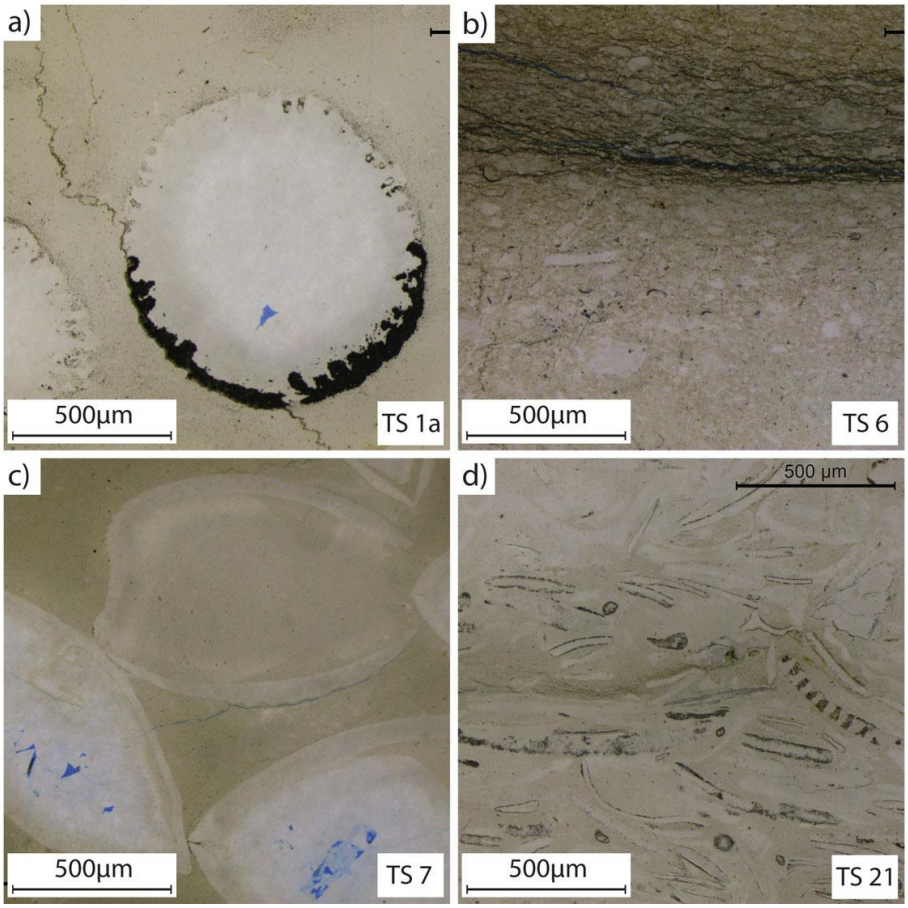

Fig: 10: Various observations of thin sections stained with blue color resin in parallel nicols. **(a)** sample TS1a (-5.6 m). Bioclastic Wackestone/Floatstone with a very fine micritic matrix. The large clasts are corals with a diameter of ca. 5 mm; **(b)** sample TS6 (2.1 m). Bioclastic micropackstone with a micritix matrix and numerous microspar. Interval at the top of the photo is laminated with a clear preferential horizontal orientation of the elongated bioclasts, whereas non-laminated interval, at the bottom of the photo, show no favored orientation of the bioclasts; **(c)** sample TS7 (-29.45 m). Floatstone with a very fine fossil-free micritic mudstone matrix. The clasts are brachiopod shells. The floatstone is actually intercalated within a micritic mudstone bed that contains nearly no bioclasts; **(d)** sample TS21 (-71.55 m). Bioclastic packstone to grainstone with a micritic matrix. This thin horizon is laminated with clasts showing a horizontal alignment. Most of the clasts are remains of bivalves but

This is the author-formatted final version of Rizzi et al. (2020), Global and Planetary Change, accepted May 4th 2020, article 103210 https://doi.org/10.1016/j.gloplacha.2020.103210

438 numerous brachiopods, gastropods are also present, along with few echinoderms and a
439 number of cup-shaped corals.

440 **5.2. Carbonate content and total organic carbon**

441 Calcium carbonate ($CaCO_3$) content varies from 13.5% up to 98.8%. The differences in
442 %$CaCO_3$ generally reflects lithological changes varying from clayey marl to limestone in both
443 small-scale and large-scale sequences (as defined below and in Figures 5 and 7). Large-scale
444 sequences, described below in chapter 5.3, are especially well-depicted by variations in
445 %CaCO3 (Fig. 11).

446 The TOC content is relatively low and varies from 0.03 % up to 1.26% with a mean
447 concentration of 0.3% (Fig. 11). TOC trends closely resemble lithological trends with
448 generally much higher concentrations in the intervals with high content of siliciclastic
449 material than in the intervals of high carbonate (Fig. 11).

450 The TOC values do not show any distinct long-term trends, but depict large-scale sequences
451 similar to those described in chapter 5.3 (Fig. 11).

452

This is the author-formatted final version of Rizzi et al. (2020), Global and Planetary Change, accepted May 4th 2020, article 103210 https://doi.org/10.1016/j.gloplacha.2020.103210

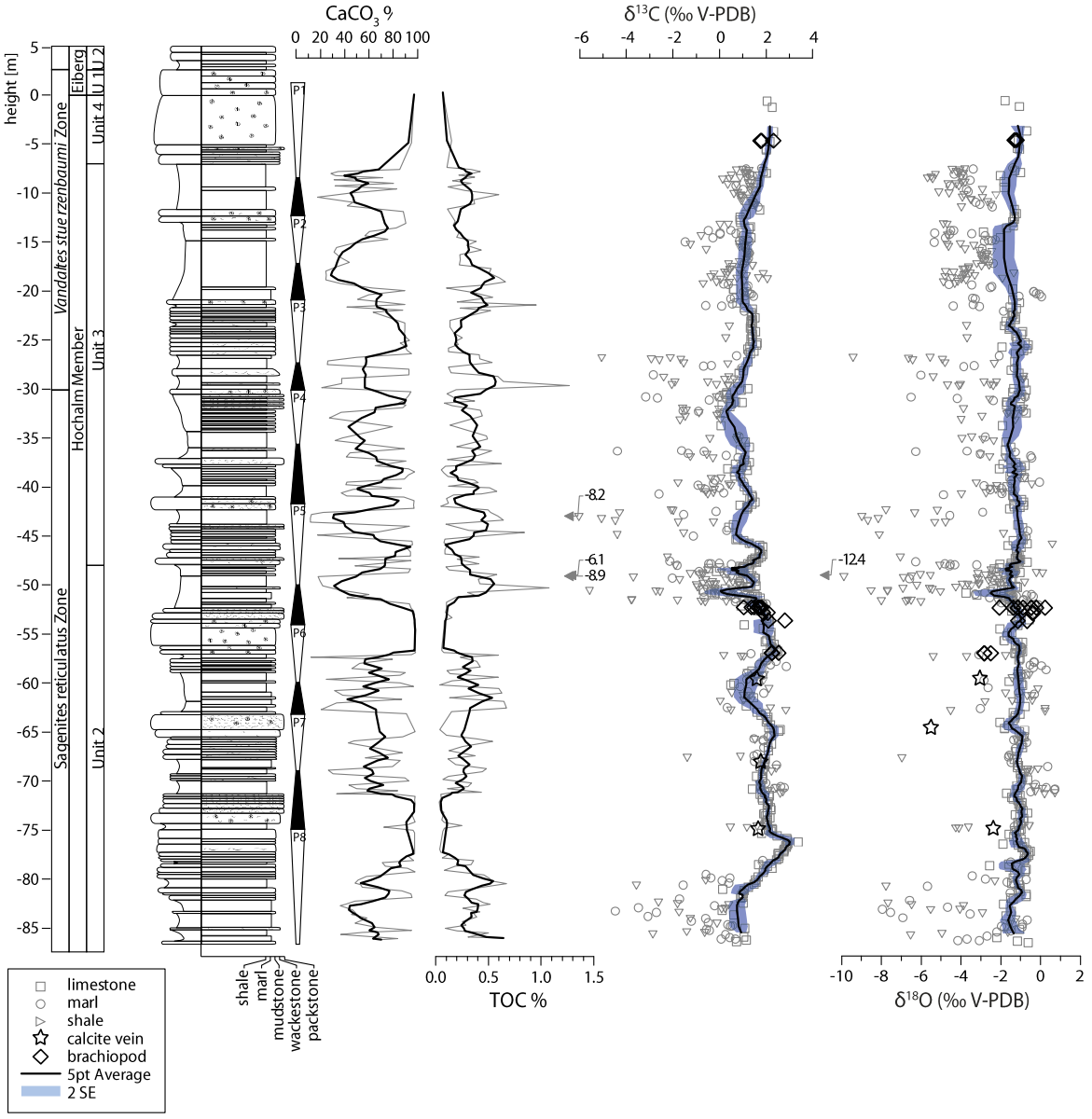

Fig. 11: Synthetic log of the Hochalm section with large-scale sequences and $CaCO_3$ content, TOC, $\delta^{13}C_{carb}$ and $\delta^{18}O_{carb}$. Average values in all the plots are calculated as 5 pt running average of the remaining dataset after removal of all the values considered as diagenetically altered (see chapter 5.4.1.). Blue envelopes represent the 2 standard error (SE) of our 5 pt window. Shales ($CaCO_3$ < 35%) are depicted as black triangles, marls ($CaCO_3$ 35% < 65%) are represented by grey circles, while limestones ($CaCO_3$ > 65%) are shown as light-grey squares.

This is the author-formatted final version of Rizzi et al. (2020), Global and Planetary Change, accepted May 4th 2020, article 103210 https://doi.org/10.1016/j.gloplacha.2020.103210

461

462 **5.3. Sequence analysis**

463 For the sequence analysis of the section, the identification of maximum flooding surfaces
464 (MFS) and transgressive surfaces (TS) is not restricted to an interpretation based on grain size
465 trends (Catuneanu *et al*., 2009). A combination of factors have been taken into account for the
466 recognition of the sequences in the section: bed stacking pattern, vertical grain-size
467 distribution, the weathering profile and carbonate content, and observed sedimentological
468 features. System tracts were defined according to the steps of Catuneanu *et al*. (2009). Since,
469 in this section the precise geochronological control is lacking, we refer to the sequences in a
470 relative sense (as recommended by Catuneanu *et al*., 2011). The depositional sequences are
471 described in the frame of a high-frequency sequence stratigraphic interpretation with the
472 transgressive surface as a lower boundary of each sequence, following Strasser (1999) and the
473 "P" parasequence concept of Schlager (2004) (Fig. 5 & 7).

474

475 **5.3.1. Small-scale sequences**

476 The small-scale sequence (small-scale sequences on Fig. 5) generally correspond to one
477 shale/marl-limestone alternation but may also be defined by a gradual increase followed by
478 a decrease in bed thickness, and/or decreasing to increasing trends in the content of the
479 siliciclastic material. Several small-scale sequences are represented by a lithological
480 alternation with its lower part characterised by an increasing trend in siliciclastic content,
481 followed by a decreasing trend in its upper part. A majority of these small-scale sequences are
482 asymmetric, with the part showing a progressive increase in siliciclastic material being
483 systematically thicker. Those trends may represent high-frequency shallowing-upward cycles
484 or variations in rates of siliciclastic and carbonate supply driven by shedding, from processes

that affected the rimmed platform and/or climatic change controlled siliciclastic sediment shedding from the Keuper region to the North (Burgess, 2001) (Fig. 5). A decrease in carbonate content is generally observed in thinning-upward mudstone beds, which are overlain by marls and shales. Conversely, an increase in carbonate mud is represented by thickening upward marl/wackestone/packstone beds, with a general increase in the amount of calcium carbonate.

A few intervals of aggradation, with monotonous/uniform lithological successions and stable trends in calcium carbonate were encountered (for example from -15 m to -20 m, Fig. 5). Placing a MFS within such successions involves a margin of error equivalent to the thickness of the condensed section (Catuneanu *et al*., 2009). Intervals with uncertainties positions of an MFS are represented by dashed lines on Figure 5.

5.3.2. Medium-scale sequences

The medium-scale sequences were determined based on the stacking of the small-scale sequences, with the aim of producing smooth sequences of relatively similar thickness. Medium-scale sequences normally start at the top of thick carbonate beds and are characterized by first an apparent deepening trend, represented by more siliciclastic deposits, followed by more carbonate-rich sediments with increasing bed thickness. Such a sequence may represent a shallowing trend but could also be the result of high-stand shedding, a process that is most pronounced on low-latitude, rimmed platforms and involves shedding of carbonate mud from the platform into the adjacent basin due to high production, rapid lithification and winnowing of the carbonate platform (Schlager *et al*., 1994) (Fig. 5).

5.3.3. Large-scale sequences

This is the author-formatted final version of Rizzi et al. (2020), Global and Planetary Change, accepted May 4th 2020, article 103210 https://doi.org/10.1016/j.gloplacha.2020.103210

The large-scale sequences in the studied succession are actually equivalent to the interpreted shallowing-upward parasequences of Golebiowski (1991) and Satterley (1996), or Transgressive-Regressive (T-R) cycles of Holstein (2004) as well as so-called "small-scale sequences" in the study of Tomašových (2006a). Each sequence consists of one interval dominated by a siliciclastic component and one dominated by carbonates. Siliciclastic intervals consist of alternating shale, marl and mudstone beds. Planar and wavy laminations occur in the lower part of these intervals and hummocky cross-stratification (HCS) is occasionally present in their topmost parts. Thin (~ 10 cm) and medium thickness (~20 cm) carbonate beds prevail in the upper part of the siliciclast-rich intervals. These intervals are well-characterised by lower $CaCO_3$ content and by enrichment in TOC (Fig. 11). The carbonate-rich intervals are characterized by thick (~0.3 m) to very thick (~5 m) carbonate beds including mudstone, wackestone, packstone or rudstone with various amounts of redeposited bioclasts (corals, sponges, brachiopod and bivalve shell debris; see also Golebiowski, 1991 and Tomašových, 2006b). These intervals are represented by the higher values in $CaCO_3$% and much lower TOC values (Fig. 11). Tomašových (2006a) argued that deposits in the carbonate-rich intervals of these sequences formed in palaeo water-depths that are not consistently above normal storm wave base (NSWB) while sediments of the siliciclastic intervals characterised by alternations of shales and thin shell beds or mudstones, sometimes bearing HCS, indicate depths above the NSWB. Therefore, he argued for alternating environmentally controlled siliciclastic versus a carbonate production and/or shedding regime to explain these sequences, rather than shallowing-upward trends. While changes in the frequency of HCS may be used as an argument for shallowing/deepening trends, the interpretation of this sedimentological feature is arguable; there are several types of HCS, produced by wave-dominated processes that occur in a wide array of proximal to

533 distal environments (Jelby *et al.*, 2020). The present study also suggests that an alternating
534 siliciclastic versus carbonate regime could have been controlled by environmental changes
535 unrelated to sealevel, across the small and medium-scale stratigraphic sequences, as also
536 suggested by the distribution of habitats in bivalves and brachiopods (Tomašových, 2006a).
537 However, the asymmetric nature of the large-scale cycles, the variations in storm intensity and
538 frequency (Golebiowski, 1991; Satterley, 1996), the stratigraphic variability in organic
539 content and palynomorphs (Holstein, 2004), and the absence of any bivalve or brachiopod
540 habitats below the maximum storm wave base (MSWB) in carbonate intervals (Tomašových,
541 2006a) support the interpretation of these sequences as shallowing-upward cycles. The
542 geological context of the large, rimmed intraplatform basin does, however, also allow for
543 other controls on facies distribution, which are further discussed in section 6 of this paper. If
544 the large-scale sequences indeed represent shallowing-upward parasequences, then it is
545 possible to position relevant surfaces. Accordingly, we placed potential maximum-flooding
546 surfaces at minimal values in the stratigraphic carbonate record, and centred within the
547 thickest shale deposits in such stratigraphic interval, which generally correspond to the middle
548 part of thick siliciclastic deposits (Fig. 5 & 7). Potential transgressive surfaces were placed on
549 the bottom of the thick (0.3 to 1.5 m) coral-bearing limestone beds and define the here
550 suggested sequence boundaries (*cf.* Strasser *et al*., 1999; Colombié & Strasser, 2003).
551
552 **5.3.4. Sedimentary succession**
553 The eight large-scale sequences consist of three to five medium-scale sequences represented
554 by meter-scale thickening upward trends, whose length varies between 1 and 4 meters
555 (Fig. 5). The oldest large-scale sequence – P8 starts at the base of the section (-86.6 m) up to
556 the top of the thick (0.6 m) mudstone bed at -74.3 m. The number and thickness of carbonate

This is the author-formatted final version of Rizzi et al. (2020), Global and Planetary Change, accepted May 4th 2020, article 103210 https://doi.org/10.1016/j.gloplacha.2020.103210

beds in this sequence is greater than in the following sequences. In the middle part of the sequence, planar lamination in the mudstone beds is observed. The P7 sequence (from -74.3 m to -64.9 m) is mainly represented by a large number of thin (5-10 cm) and medium (10-20 cm) carbonate beds intercalated with shales and marls. In the top of the sequence, some of the mudstone beds contain HCS and normal gradation of the grains (Fig. 5).

Sequence P6 (-64.9 m to -57 m) is also mainly represented by thin and medium (5-20 cm) carbonate beds intercalated with shales and marls, which in this case are prevailing. This sequence starts with coral rudstone and ends with a shelly rudstone. HCS occurs in its upper part.

Sequence P5 (-57 m to -42.3 m) starts with thin to medium (10-15 cm) beds of coral-bearing limestone with a high number of coral fragments, progressively grading into thicker beds. A thick coral rudstone and shelly wackestone beds, containing fewer shells follow. Progressively thicker siliciclastic intervals occur at the top. The middle part of P5 is characterized by an increasing amount of thin and medium (5-15 cm) mudstone and wackestone beds, some containing wavy and planar lamination. This is followed by a thick (1.35 m) shaly interval with planar lamination throughout. The sequence ends at the base of two beds of coral-bearing limestone.

Sequence P4 (-42.3 m to -30.6 m) is characterized in its lower and middle part by mainly siliciclastic sediments, while towards the top, the amount of carbonate beds increases. Mudstone beds, occurring in the upper half of the siliciclastic interval, have constant thickness of about 10 cm, and are overlain by a thick (50 cm) wackestone bed. In the topmost part of sequence P4 calcareous sediments are represented by shelly packestone beds, with wavy laminations.

This is the author-formatted final version of Rizzi et al. (2020), Global and Planetary Change, accepted May 4th 2020, article 103210 https://doi.org/10.1016/j.gloplacha.2020.103210

Sequence P3 (-30.6 m to -21.2 m) starts with a coral-bearing wackestone with wavy laminations and shells. This sequence is characterized in its lower half by shales intercalated with few, thin (10 cm) mudstone beds. One exception in this interval is a thick (70 cm) wackestone to mudstone bed with dispersed shells in the basal part and HCS in the middle. The upper half of the sequence shows medium to thick (20-40 cm) mudstone beds with wavy laminations intercalated with few medium (10-20 cm) shale beds. The sequence ends at the bottom of a 30 cm thick coral-bearing and shelly rudstone.

Sequence P2 (-21.2 m to -12.9 m) consists mainly of siliciclastic deposits. In this sequence, the sedimentological record alone does not allow a clear recognition of potential genetic and medium-scale sequences because of the presence of a very long (4.8 m), uniform, shaly interval. Regular changes in the color of the shales, however suggest changing conditions, which can also be seen by a detailed analysis of medium-scale sequences in the isotope record, $CaCO_3$ content and TOC (Fig. 11). Two medium-scale sequences are identified in the uppermost part of the sedimentary sequence and the identification of three additional medium-scale sequences have been justified in the lower part using the chemical data. Sparse mudstone beds characterize the uppermost part of the sequence, which ends at the bottom of the first wackestone bed with coral fragments.

Sequence P1 (-12.9 m to -5 m) starts with four progressively thicker (up to 40 cm) wackestone beds with loosely distributed shells and coral fragments. This sequence is again dominated by siliciclastic sediments in its bottom half. In this sequence the number of thin to medium bedded limestone beds, and bioclasts (shells, corals) increases towards the top so that a progressive change from mudstone to packstone is observed. This sequence ends with few thin rudstone beds containing corals and shells under a very thick (5 m) coral-bearing

603 rudstone that corresponds to the Korallenkalk, which defines the Hochalm Mb Unit 4 of
604 Golebiowski (1991).
605 Generally, even though the relative proportion of the observed lithofacies types varies, all five
606 kinds of lithofacies can be found in each of the sequences. Shales, marls and mudstones
607 prevail in the siliciclastic sequences, but thin carbonate beds with bioclasts may also occur in
608 those intervals. In the carbonate intervals, bioclastic wackestone, packstones, rudstones and
609 mudstones prevail.
610

611 **5.4. Stable isotopes**

612 **5.4.1. Preservation of the stable isotope data**

613 The carbonate carbon isotope record shows variations ranging from -8.9‰ to +3.4‰ (Fig.
614 11). The lightest values are observed in shale and marl samples, whereas in limestones,
615 $\delta^{13}C$ values are much heavier and less scattered (Fig. 12).
616 The $\delta^{18}O$ values vary considerably between -12.4‰ and +0.7‰. Oxygen isotope ratios, like
617 $\delta^{13}C$, show strongly reduced variability in the limestone samples, ranging from -3.8‰ to -
618 0.5‰, and fluctuating around a relatively stable average of -1.3‰.
619 Preservation assessment of the $\delta^{13}C_{carb}$ and $\delta^{18}O_{carb}$ values is presented in the cross plots in
620 Figure 12. We first adopted a similar approach to that of Farouk *et al*. (2018) looking at
621 patterns of the overall distribution of $\delta^{13}C_{carb}$ values. The distribution histogram of $\delta^{13}C_{carb}$
622 data shows a strong deviation from a normal distribution with skewness on the left part of the
623 graph toward lighter values as well as multiple modes (Fig. 12a). This statistical distribution
624 suggests a large cluster of data > -1‰ and a long tail of altered values < -1‰. A cross-plot of
625 $\delta^{13}C_{carb}$ and $\delta^{18}O_{carb}$ values (Fig. 12b) also highlights a typical positive covariance between the
626 two parameters expected in mixing lines produced by the addition of variable amounts of

627 isotopically heterogeneous diagenetic cements with lighter values to the isotopically
628 homogeneous primary values of the calcite (Jenkyns, 1995; Mitchell *et al*., 1997). Reducing
629 the total dataset to $\delta^{13}C_{carb}$ values > -1‰ reduces the correlation coefficient between the two
630 parameters although it remains significant at p <0.01, which suggests that there may be a
631 diagenetic impact on some of the remaining data (Fig. 12b). A cross-plot of $\delta^{18}O_{carb}$ and
632 $\%CaCO_3$ values (Fig. 12c) shows a clear cluster of many values around a mean of -1.3‰ in
633 oxygen with very high carbonate content (> 80%). Oxygen isotope values between 60% and
634 80% in $CaCO_3$ do not look profoundly different but once the threshold of 60% is passed,
635 values in $\delta^{18}O_{carb}$ show a much wider spread toward either much lighter or heavier values
636 (Fig. 12c). A similar threshold of 60% in $CaCO_3$ also allows to filter out all $\delta^{13}C_{carb}$ data < -
637 1‰ (Fig. 12d). Finally, cross-plots of $\delta^{18}O_{carb}$ data versus TOC and $\delta^{13}C_{carb}$ data versus TOC
638 do not delineate any clear link between influences from a potential decay of organic matter on
639 the $\delta^{13}C_{carb}$. However, the samples with a high $CaCO_3$ concentrations and $\delta^{18}O_{carb}$ values
640 around -1.3‰ (grey cluster in Fig. 12c) group similarly in the plot TOC vs. $\delta^{18}O_{carb}$ (grey
641 cluster in Fig. 12e) – the data in the clusters of both figures originate from the same samples.
642 Taken all together, these results indicate a significant impact of diagenesis in the isotopic
643 dataset for marly and shaly lithologies with a threshold at 60% in $CaCO_3$. Consequently,
644 culling potentially altered data has reduced the original dataset. Only isotope data derived
645 from the limestones (i.e. lithologies > 60% in $CaCO_3$) have been kept and will be discussed
646 subsequently. To further reduce the noise, a 5-point average and 2 standard-deviation (sd)
647 envelope were calculated (Fig. 13).
648 Most of the bulk organic carbon isotope record shows variations ranging from -29‰ to
649 -24.7‰ (Fig. 13). High-frequency variations are generally rather small, and only in few
650 instances reach up to 2.9‰. This spread of the values could be explained by the possible

This is the author-formatted final version of Rizzi et al. (2020), Global and Planetary Change, accepted May 4th 2020, article 103210 https://doi.org/10.1016/j.gloplacha.2020.103210

influence of early sedimentary diagenesis that can alter the isotopic signal for up to 1.5‰ (McArthur *et al*., 1992). Moreover, carbon isotope signals are generally quite resistant to diagenesis and constitute an excellent correlation tool throughout Earth history (Meyers, 1993; Saltzman and Thomas, 2012). Preservation of the Brachiopod shells was assessed by microscopy.

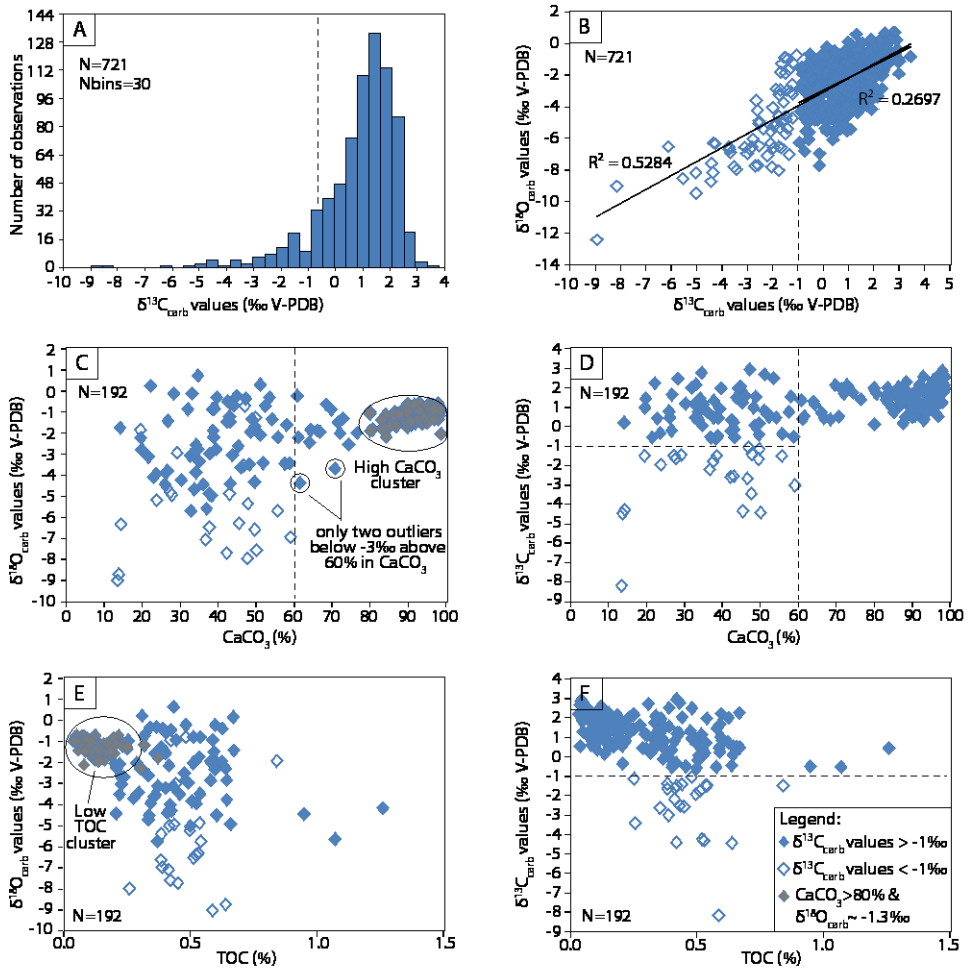

Fig. 12: Various plots showing preservation and the potential impact of diagenesis on the stable isotope data. **(a)** distribution histogram of $\delta^{13}C_{carb}$ values; **(b)** cross-plot of $\delta^{13}C_{carb}$ and $\delta^{18}O_{carb}$ values; **(c)** cross-plot of $\delta^{18}O_{carb}$ and $\%CaCO_3$ values; **(d)** cross-plot of $\delta^{18}C_{carb}$ and $\%CaCO_3$ values; **(e)** cross-plot of $\delta^{18}O_{carb}$ data versus TOC; **(f)** cross-plots of $\delta^{18}C_{carb}$ data versus TOC. The dashed lines mark threshold of 60% in $CaCO_3$ and -1‰ in $\delta^{13}C_{carb}$ data. For more information see text.

This is the author-formatted final version of Rizzi et al. (2020), Global and Planetary Change, accepted May 4th 2020, article 103210 https://doi.org/10.1016/j.gloplacha.2020.103210

670

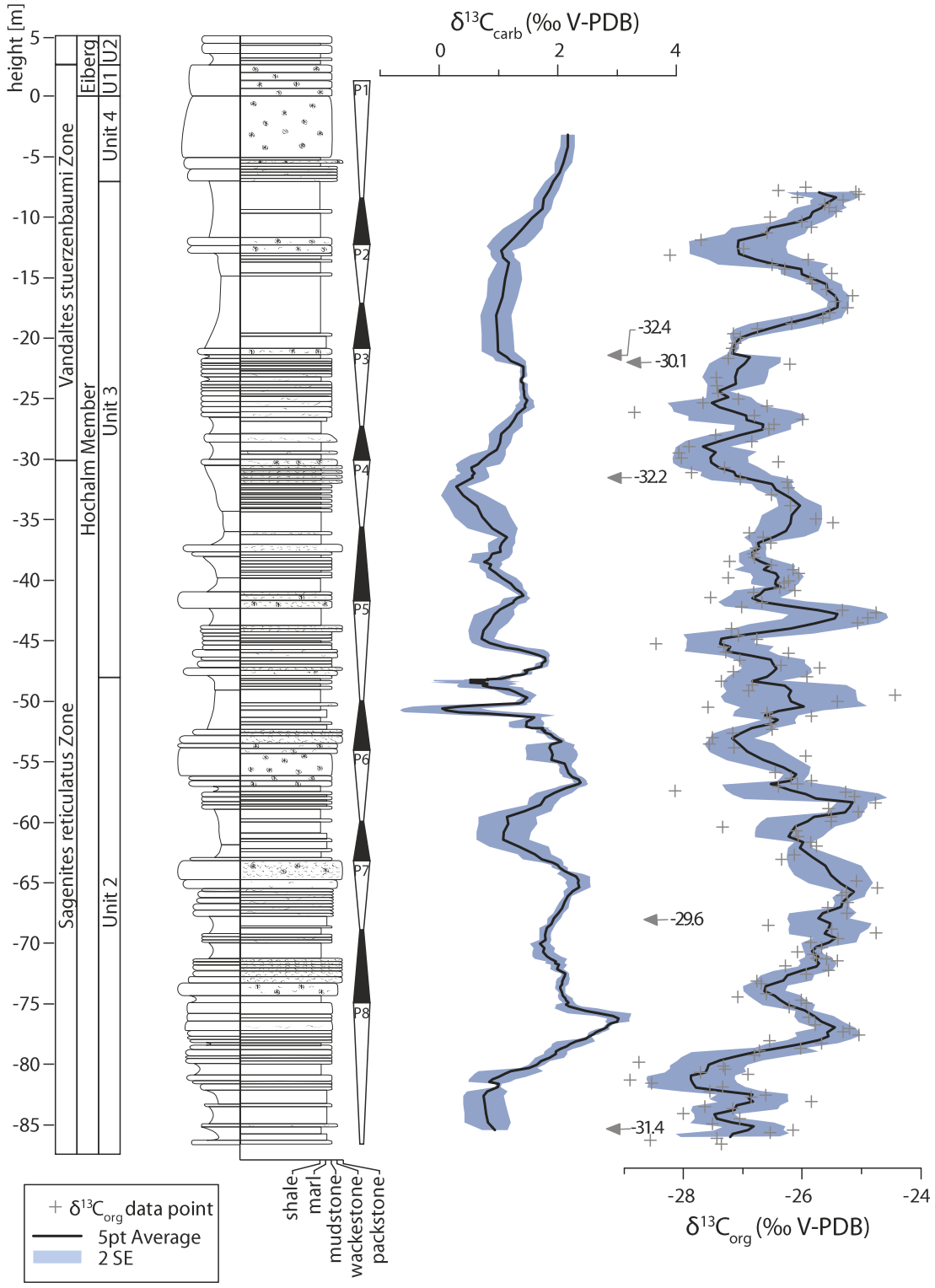

671

672 **Fig. 13:** Synthetic log of the Hochalm section with the cleaned $\delta^{13}C_{carb}$ curve compared to

673 data obtained on $\delta^{13}C_{org}$. In plots, average values are a 5 pt running mean, while envelopes

represent the 2 standard error (SE) over a 5 pt moving window (5 values < -29.5 ‰ in $\delta^{13}C_{org}$ were considered as outliers and excluded for the calculation of the 5 pt mean).

5.4.2. Bulk carbonate carbon and oxygen isotope trends

Besides several smaller-scale superimposed isotopic fluctuations in the profile (of around 1‰), three long-lasting trends can be recognized. Between -85 m and -77 m a prominent (from ~1.2‰ to ~3‰) positive shift occurs (Fig. 13). The carbon isotope values show subsequently a fluctuating negative trend in the higher part of Unit 2 (starting at -77 m) and during the lower and middle Unit 3 reaching values of ~0‰ at -32 m. The $\delta^{13}C$ values increase subsequently from the middle part of Unit 3 and continuing into Unit 4 from 0.6‰ to 1.9‰. The $\delta^{13}C$ values from calcite veins and fossil shells closely resemble the values of the bulk rocks of the same beds (Fig.11).

Diagenetically-screened oxygen isotope data fluctuate around a relatively stable average of -1.3‰. In some distinct intervals $\delta^{18}O$ values of marl and shale samples are heavier than those of close-by limestone samples, especially in the lower half of the investigated succession (c. -70 m, -60 m and -50 m).

Brachiopod data generally show compatible or slightly heavier values than those from the bulk limestones of the same beds (Fig.11).

5.4.3 Bulk organic carbon isotopes ($\delta^{13}C_{org}$)

Long-lasting $\delta^{13}C_{org}$ trends are similar to those of $\delta^{13}C_{carb}$, but small-scale fluctuations are superimposed on them. The $\delta^{13}C_{org}$ data varies between -32.4‰ to -24.7‰. However, only six stratigraphically separated values are lighter than < -29‰ (Fig. 13). Due to their scattered nature these light values were not taken into consideration while reconstructing palaeoenvironmental conditions. At the base of the section in Unit 2, the mean values show

minimum of -27.5‰ followed by a more than 2‰ increase and subsequently by fluctuating values around -26‰ until -57 m. The values drop then, at the beginning of Unit 3 (up to -32 m), by more than 1‰ to about -27.7‰. The $\delta^{13}C_{org}$ shows a general positive trend by more than 2‰ from -32 m to the top of Unit 3 reaching values of -25.7‰.

6. Discussion

6.1. Depositional environments

Sediments of the Kössen Formation show abrupt, repetitive changes from organic-rich shales and marls to carbonate intervals and reflect the typical array of different environments occurring in shallow intraplatform lagoons or backplatform basins. As described in detail above and documented by Golebiowski (1990, 1991), Holstein (2004) and Tomašových (2006a), periodic changes in lithology document a series of well-defined shallowing-upward sequences or parasequences. The absence of any indication for subaerial exposure suggests that (1) relatively continuous sedimentation occurred in the basin and (2) the general trend observed toward a higher siliciclastic input reflects either a long-term transgression that eventually led up to a much wider basin and the emergence of deeper facies in the Eiberg Member (Golebiowski, 1990, 1991), or an enhanced siliciclastic input favoured by a more humid climate across the lower to middle Rhaetian. According to Golebiowski's interpretation, recognized depositional sequences in the Hochalm section indicate that high frequency and low-amplitude sea level change may have controlled accommodation space in the basin. Whether, these depositional sequences are related to orbital forcing remains yet to be constrained, since the depositional setting in a shallow intraplatform basin can easily lead to lateral variations in facies. Furthermore, in such a depositional setting it is likely that the sedimentological record is fragmentary. Therefore, it cannot be excluded that some of the

small-scale and medium-scale sequences reflect coastline-parallel, lateral change from a siliciclastic-dominated to carbonate-dominated environment. In Golebiowski's original depositional model, sedimentation of the Hochalm Mb. took place in a shallow intraplatform basin, which was delimited to the south-east by a rim with patch reefs nowadays represented by the Steinplatte Kalk (which is part of the Dachsteinkalk complex). Towards the north-west there was a possible gradual transition to the Keuper Facies. Despite the absence of any facies transition between the Kössen Facies and the Keuper Facies (no such outcrops have been found so far), it seems probable that the relatively high amount of fine-grained siliciclastics, and the occurrence of shales in the Kössen Formation, was due to fluvial/aeolian input from the Germanic Basin to the north-west.

Accordingly, Golebiowski (1990) considered that carbonate production was probably concentrated at the southeastern margin of the basin, in relative shallow water. The deposition of carbonate would decrease towards the northwest with increasing distance from the rim and increasing water depth. In this model, the large-scale depositional sequences are controlled by relative sea-level fluctuations, with carbonate production shifting along a SE-NW trend. However, this model does not take into account the consistent presence of coral debris at the top of each of our 8 large-scale sequences, which supports the development of small patch-reefs (low-diversity of the corals and absence of sponges, microbial crusts and isopachous cements advocate against the development of a proper upper Triassic reef system). Because corals require light and clear waters to grow (Pandolfi, 2011) non- or low turbid environments may have promoted their development.

Some of the beds in the studied section are characterized by grading and sorting (such as tempestite beds), indicating storm activity. However, the massive carbonate beds that occur at the top of the shallowing sequences show no signs of sorting. If these beds cannot be

746 connected to high storm intensity, this would argue against the theory of Tomašových (2006
747 a, b) on strong changes in storm intensities mediating the changes in carbonate to siliciclastic
748 deposition. Alternatively, following Tomašových's model, carbonate debris are essentially
749 transported by storms through the basin. Hence, following this model, variations in
750 siliciclastic/carbonate deposition may have resulted from variations in the amount of
751 carbonate production on the platform, or silicate weathering or relative changes in subsidence
752 between the areas of siliciclastic and carbonate deposition.
753 Another model for the formation of large-scale sequences in the Eiberg Basin at that time
754 arises from the work of Tomašových (2006a). This author suggested that both facies and the
755 bivalves and brachiopod content point to depositional environments of the Hochalm section
756 situated always below the fair weather wave base (FWWB), with many facies situated below
757 the NSBW, which is generally below the euphotic zone where hermatypic corals are less
758 abundant. In this model, siliciclastic and carbonate-dominated intervals are independent from
759 depth trends, but strictly controlled by changes in climate, and particularly humidity, with
760 humid climates favoring the siliciclastic and nutrient inputs to the basin. In this model,
761 highstand shedding is a process that would vary in intensity (Fig. 15). Arid periods limiting
762 freshwater and siliclastic input may have favored the development of shoal and reefal
763 carbonates whose debris were exported into the Kössen Basin. Ostracods and eurytopic
764 bivalve associations of units 2 and 3 indicate adverse salinity conditions in the Hochalm
765 Member (Urlichs 1972, Golebiowski, 1989), and thus support restricted conditions with
766 significant changes in salinity.
767
768 The bioclastic packstones (L3), recognized in thin-sections TS 13 (-44.7 m, Fig. 8g) and TS
769 12 (-50.3 m, Fig. 8e and f), reflect most probably the margin of carbonate sand bar (shoals)

depositional environments affected by wave action (Fig. 14). The presence of involutinid foraminifers support this interpretation, as these late Triassic foraminifers mostly proliferated in peri-reefal environments and have often been transported by storms towards deeper areas between the fair-weather wave base and the storm weather wave base (Somma *et al.*, 2010). However, transport (reworking) of benthic foraminifers by storms cannot be excluded, hence this facies may simply represent a typical carbonate storm deposit situated in deeper environments between the NSWB and the FWWB (Tomašových, 2006a; Fig. 15).

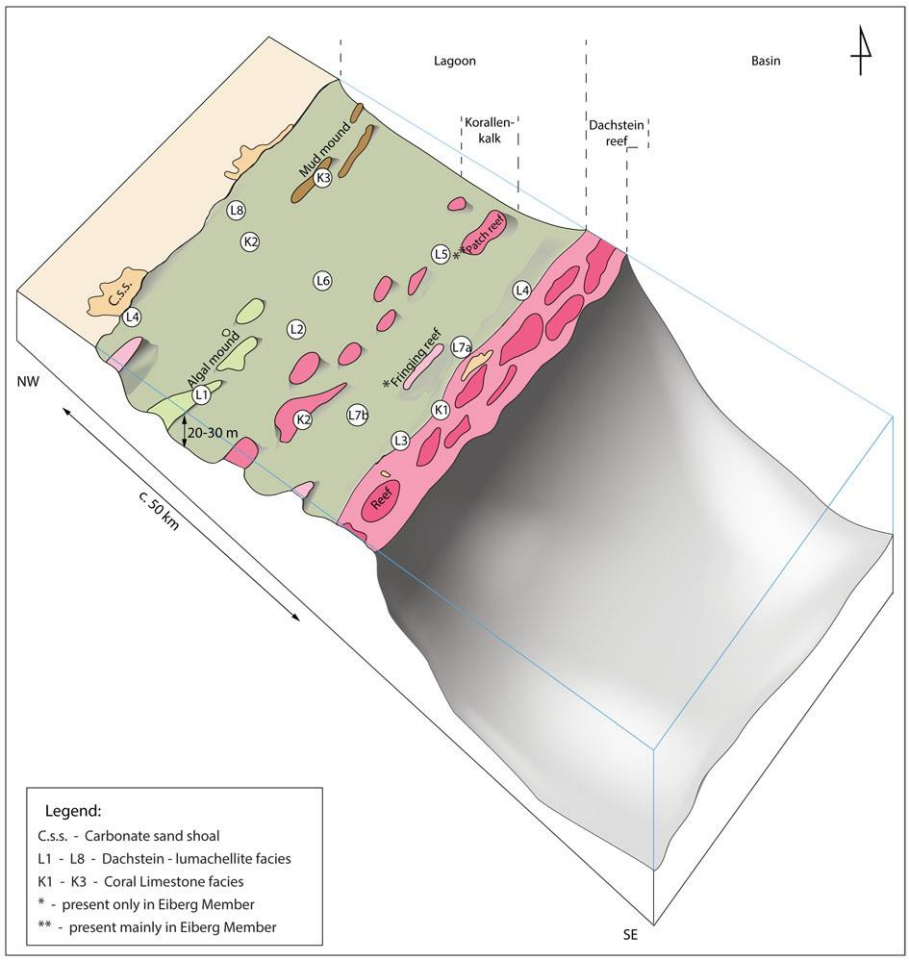

Fig. 14: 3D diagram representing a paleoenvironmental model of deposition of the Eiberg Basin for the Eiberg and Hochalm Mb based on the original model of Golebiowski (1991) with the supposed environmental interpretations of his various facies. Features that were present only during the deposition of the Eiberg Member, but not attested in the Hochalm

Member are marked with a star. The various microfacies correspond to those described in Appendix A: **L1 -** Laminated algal bindstone; **L2 -** Peloidal pack/gainstone; **L3 -** Bioclastic packstone; **L4 -** Oolite facies; **L5** - Foraminiferal wacke/packstone; **L6 -** Mudstone facies; **L7a** - Proximal tempestite facies; **L7b -** Distal tempestite facies; **L8 -** Oncoid-detritus facies; **K1 -** Coral detritus mud facies; **K2 -** Biostrome facies; **K3 -** Mud mount facies

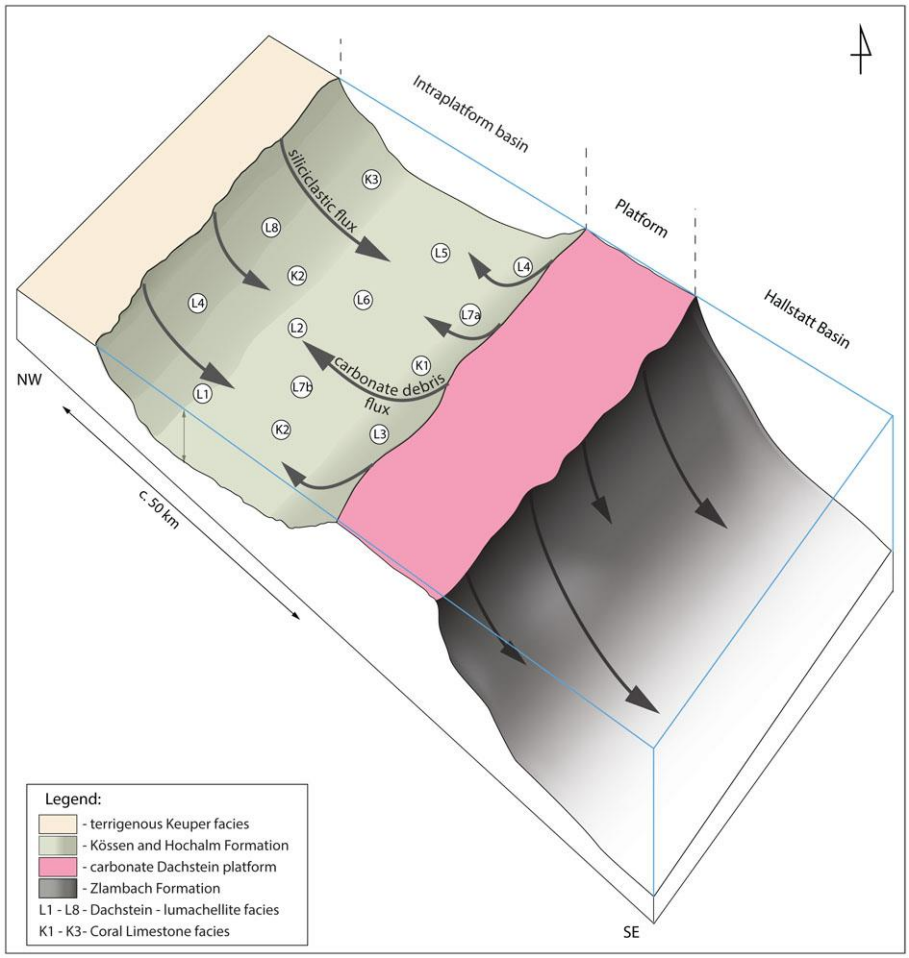

Fig. 15: 3D diagram representing a model based Tomašových (2006a). This model (modified from Meschede, (2015)) implies that changes from carbonate to siliciclastic deposits were caused via a climatic control on storm intensity, platform erosion, and the capacity of platform-derived carbonate transported to the basin interiors to dilute siliciclastic material. The siliciclastic material would be delivered from the NW and the carbonate debris from the

Dachstein platform in the SE. In this model, Facies K1 to K3 and L1 to L8 (see Fig. 14) do not necessarily represent any specific environments of the Basin and may represent variations from the type of carbonate debris brought from the Dachstein platform.

Laminated mudstones (L6a) and non-laminated fossil-free fine mudstones occurring throughout the succession are associated with higher values in TOC, and recognized in thin section TS 10 (-55.86 m, Fig. 8c). Such facies were deposited in a strongly restricted basin with anoxic deeper waters, an environment where higher concentrations of organic matter is generally preserved (Fig. 14).

Proximal tempestite facies (L7a), represented by thin section TS 21 (-71.55 m, Fig. 8a, b and 10d), were deposited in subtidal environment. This is supported by the distribution of micritic matrix and peloids in the sample (Table 1).

Distal tempestite facies (L7b) were recognized in sample TS 6 (2.1 m, Fig. 9g, h and 10b) and TS 7 (-29.45 m, Fig.8h and 10c). In sample TS 6, laminated intervals with horizontal orientation of the elongated clasts are intercalating with intervals with no favored orientation. These features are characteristic of a change in hydrodynamic conditions from high to low and can be associated with storm deposits. Also, accumulation of the single layer of shells recognized in thin section TS 7 (Fig. 10c) points towards a deposition occurring in calm water areas, below the fair weather wave base (Fig. 14). The involutinid foraminifers found in the infilled micritic matrix of one of the brachiopods (Fig. 8h) could have been transported during higher energy events, e.g., storm currents moving from shallower towards deeper water.

Coral detritus mud facies (K1) occurs at the top of Unit 4 of the Hochalm Mb (TS2, TS 3 and TS 4 at 4.75 m, 3.75 m, -0.65 m respectively; Fig. 9b, c and d respectively). Low diversity of the bioclasts, and poor sorting of the material could point towards deposition in a shallow

environment, in the vicinity of the reef or to a lagoonal setting with some solitary corals (Fig. 14). It cannot be excluded that this facies also represents the expression of a particularly arid period that limited nutrient export and turbidity of waters, and which favored the development of reefal corals subjected to winnowing and transport to the basin.

The biostrome facies (K2) identified in thin sections TS 1a (-5.6 m, Fig. 9a and 10a) and TS 11 (-52.65 m, Fig. 8d) depict slightly reworked coral fragments embedded in a fine matrix. This facies was accumulated below the fair-weather wave base in the vicinity of patch reefs (Fig. 14).

The echinoderm detritus facies (D1) is represented by samples TS5 (15 cm, Fig. 9e) and TS5b (-1m, Fig. 9f). Deposition of this poorly sorted wacke-/packstone with majority of the debris consisting of echinoderms fragments occurred in a deeper basinal environment and attest of a profound modification in the Eiberg Basin which was interpreted by Golebiowski (1989) as a major middle Rhaetian transgression (Fig. 6).

6.2. Evolution of facies and environments through time

Our study illustrates the overall evolution of facies previously described by Golebiowski (1991) in the Northern Calcareous Alps where facies met in Unit 2 primarily represent the "Lumachellen realm", facies of Unit 3 correspond mostly to the detrital lagoon of the Korallenkalk realm and facies of Unit 4 correspond to a large, regionally well-developed Korallenkalk patch- to fringing-reef (Golebiowski, 1991). Facies characteristic of the detritus mud carbonate realm were only observed in the topmost part of the section, in concordance with Golebiowski's interpretation of a much wider and deeper basin for the Eiberg Mb (Fig. 6). This earlier interpretation may suggest a progressive evolution of facies from very shallow environments of carbonate shoals characteristic of the "Lumachellen realm" to facies

842 of the detritic lagoon already at the top of Unit 2 (Fig. 5). Evolution from a mostly shallow
843 lagoon to a deeper and wider rimmed intraplatform basin may have been favored by
844 transgression. The deepening of this lagoon was immediately followed by the development of
845 the large Korallenkalk fringing reef (Fig. 5). In accordance with Golebiowski's (1991)
846 interpretation, the following deepening-upward trend that characterizes Unit 1 and Unit 2 of
847 the Eiberg Mb allowed for a return to the development of deeper carbonate facies as recorded
848 herein. However, as described above, many of these facies point to storm deposition involving
849 transport and export of carbonate mud. Following Tomašových's (2006a) interpretation,
850 facies variations as well as long-term trends may simply reflect changes in nutrient, turbidity
851 and siliciclastic influx controlled by variations in humidity (Fig. 15). In this model,
852 siliciclastic-dominated intervals represent more humid periods when the weathering of
853 continental hinterlands supported a high detrital flux and enhanced nutrient delivery. The
854 carbonate-dominated intervals represent more arid periods that favored the development of
855 oligotrophic reefal systems and carbonate shoals subjected to erosion and winnowing that
856 favored the process of highstand shedding. This latter interpretation opens interesting
857 perspectives regarding the nature of our eight parasequences. If the observed sequences were
858 essentially controlled by changes in humidity, then they likely represent the expression of a
859 changing insolation, and hence of a likely orbital control on sedimentation. The thickness-
860 ratio between the large-scale and medium-scale sequences varies between 1:4 and 1:6. Even
861 though this variable range of ratios may be suggestive of the expected range of ratios of short-
862 eccentricity to precession, we cannot exclude bundling of short-eccentricity into long-
863 eccentricity cycles. Moreover, we remain cautious here with an orbital interpretation of our
864 parasequences as environments with preponderant transport and redeposition, wave-

865 dominated and gravity-settling deposits can be poorly suited for a non-ambiguous recognition
866 of orbital cycles.
867
868 **6.3. Carbon isotope stratigraphy**
869 Paleoenvironments such as those characterised in the Hochalm succession imply multiple
870 sources of carbonates, i.e. a mix of micritic mud and abundant debris of various macrofossil
871 shells, some of which were deposited in shallow environments whereas others were deposited
872 offshore. These different constituents potentially bear distinct carbon isotope signatures due to
873 their distinct origins across a variety of proximal to distal settings. However, it has been
874 shown that even for shallow platform carbonate environments it is possible to record well-
875 preserved, global carbon-isotope trends. Previous studies of Embry *et al*. (2010) and Huck *et*
876 *al*. (2011, 2013) have demonstrated that the carbon-isotope signature of bulk and micritic
877 shoal carbonates can reflect global long-term trends, which can be correlated to deeper parts
878 of carbonate basins. The new high-resolution carbonate carbon isotope record may thus prove
879 useful for correlation of the Rhaetian stage. However, the five short-term negative excursions
880 (minima at -60 m, -50 m, -40 m, -30 m, -18 m; Fig. 13) in the $\delta^{13}C_{carb}$ record of the Hochalm
881 section may represent diagenetic features. These negative excursions are associated with the
882 siliciclastic intervals, with low to very low $CaCO_3$ content, and therefore may be related to
883 deeper water deposits. Since sea level changes were limited in the area (Satterley, 1996;
884 Tanner, 2010) input of the lighter ^{13}C from the open ocean waters is unlikely. This
885 interpretation is supported by the organic carbon isotope record that does not show any of
886 these short-term negative $\delta^{13}C_{carb}$ fluctuations (Fig. 13), whereas they should be expressed in
887 the $\delta^{13}C_{org}$ if they were to represent global carbon-cycle change. Furthermore, a diagenetic
888 signature is particularly prevalent in samples with low carbonate content, therefore in

889 siliciclastic intervals, as inferred from isotopic covariation and strongly depleted isotopic
890 values. All these observations indicate that the short-term negative carbonate $\delta^{13}C$ excursions
891 do not reflect primary signals, but rather represent a diagenetic signature in the mostly
892 siliciclastic intervals; these lighter data, however, could have been missed by our standard
893 diagenetic screening (see section 5.4.1; see also Veizer, 1983; Marshall 1992; Ullmann &
894 Korte 2015; and discussion in Veizer *et al*., 1999). In contrast, a positive trend in bulk
895 carbonate carbon isotopes of about +3‰ at the base of the section (from minimum at c. -85 m
896 to maximum at -77 m) is defined mostly by limestone values. These diagenetically screened
897 limestone data, generally correspond to the $\delta^{13}C$ data from brachiopods which have passed the
898 diagenetic screening, do not show high frequency oscillations or strongly negative $\delta^{13}C_{carb}$
899 (and $\delta^{18}O_{carb}$) values and are therefore likely to reflect the primary palaeoenvironmental
900 information. Additionally, this pronounced positive carbon isotope trend is also expressed in
901 bulk $\delta^{13}C_{org}$ (Fig. 13) and therefore most likely represent a significant primary trend. This
902 isotopic event potentially constitutes an important stratigraphic marker that may be compared
903 with the low-resolution carbon isotope dataset from Rhaetian brachiopods and bulk
904 carbonates of the NCA with values ranging between 2‰ and 3‰ (Korte *et al*., 2005; Krystyn
905 *et al*., 2007). The results of the latter indicate that the significant positive trend from the new
906 dataset (Fig. 13) might represent a new chemostratigraphic marker that was not identified
907 clearly in previous low-resolution datasets (Korte *et al*., 2005) and could represent another
908 carbon cycle perturbation of the Rhaetian preceding the ETME (see Ruhl & Kürschner, 2011;
909 Mette *et al*., 2012). It remains unclear whether this marked increase in carbon isotopes is a
910 feature that is essentially prescribed to the lower Rhaetian or whether it could represent the
911 recovery part of a Norian/Rhaetian negative excursion previously identified by several authors
912 (Preto et al., 2013; Muttoni et al., 2014; Maron et al., 2015; Zaffani et al., 2017). The longer

lasting slight decrease of the carbonate carbon isotopes from the upper part of Unit 2 to the middle of Unit 3, as well as the > 1‰ increase in the upper part of Unit 3 and within Unit 4 is paralleled by trends in $\delta^{13}C_{org}$. This suggests that these fluctuations are also primary in nature (Fig. 13) and can be used in refining the stratigraphy of the Rhaetian stage. The integration of data from bulk organic matter, bulk carbonates, brachiopods, and the diagenetic screening applied here make our new dataset one of the most robust Rhaetian carbon isotope record thus far.

7. Conclusions

In this study, we investigated the evolution of sedimentary facies and the carbon isotope stratigraphy of the lower to middle Rhaetian Hochalm section, which constitutes a key succession for the Late Triassic of the Northern Calcareous Alps. Our study led us to identify eight 10 to 15 m thick apparent shallowing-deepening sequences, or 'parasequences' that we associate either with relative sea-level change, either with changes in the hydrological cycle. Each of these sequences is characterised by siliciclastic intervals, generally slightly enriched in organic matter and exhibiting microfacies that are characteristic of high energy deposits and/or detrital intraplatform basin deposits whereas lime intervals show systematic enrichments in coral debris and other bioclasts associated to patch reefs. Our sedimentological study illustrates previous interpretations of an overall evolution from (1) a highly energetic shallow lagoon in the lower Rhaetian (Hochalm Mb Unit 2), so-called 'Lumachellen realm' to (2) a slightly deeper detritic lagoon with development of patch and fringing reefs, so-called 'Korallenkalk realm' in the lower to middle Rhaetian transition (Hochalm Mb Unit 3), followed by (3) the establishment of a large regional fringing reef in the late middle Rhaetian

(Hochalm Mb Unit 4). This latter reef or 'Korallenkalk' was established immediately after a profound change in the shape of the Eiberg Basin toward a wider and deeper basin, which was possibly caused by a major transgression. However, more recent interpretations based on brachiopod and bivalve assemblages support an origin of parasequences from changes in humidity, causing variations in the siliciclastic and nutrient fluxes and associated water turbidity, as well as varying intensities of highstand shedding. If climate change was the primary control on storm-intensity and variations in siliciclastics and carbonate mud, then it is likely that the eight identified parasequences represent an orbital control on insolation. The variety of encountered facies allowed us to draw a paleoenvironmental model of deposition for the Hochalm Mb. Despite the variety of facies encountered, carbon isotope stratigraphy established on bulk carbonate, brachiopod calcite and bulk organics allowed us to delineate common trends. Our signals show a transient ~3‰ rise in carbon isotopes in the Lower Rhaetian (Hochalm Mb Unit 2), followed by a long-term 1.5‰ to 2‰ decrease up to the lower part of the middle Rhaetian, further followed by a subtle ~1‰ to 1.5‰ increase at the top of the Hochalm Mb. It remains unclear whether the transient positive excursion in carbon isotopes identified at the base of the section represents a trend restrained to the Rhaetian or the recovery of a negative Norian/Rhaetian excursion. Nevertheless, the integration of data from bulk organic matter, bulk carbonates, brachiopods, and diagenetic screening applied here make our new dataset one of the most robust Rhaetian carbon isotope record thus far. Such trends may help refining the stratigraphy of the Rhaetian stage.

Acknowledgements

We acknowledge the Carlsberg Foundation (project 2009-01-0759 provided for C.K.), the Danish Council for Independent Research–Natural Sciences (project 09-072715 provided for

This is the author-formatted final version of Rizzi et al. (2020), Global and Planetary Change, accepted May 4th 2020, article 103210 https://doi.org/10.1016/j.gloplacha.2020.103210

961 C.K.) and the Austrian Science Fund FWF (project 25782-B16 provided for W.M.) for
962 contributions to financing this project. Many thanks to Stefan Spreng and the Bayerischer
963 Saalforst Unken for access to, and logistical support in the field. We thank Sylvain Richoz
964 and an anonymous reviewer for their comments that significantly improved our manuscript.
965

This is the author-formatted final version of Rizzi et al. (2020), Global and Planetary Change, accepted May 4th 2020, article 103210 https://doi.org/10.1016/j.gloplacha.2020.103210

References

Ahlberg, A., Arndorff, L., & Guy‐Ohlson, D. (2002). Onshore climate change during the Late Triassic marine inundation of the Central European Basin. Terra Nova, 14(4), 241-248.

Balogh, K. (1981). Correlation of the Hungarian Triassic. *Acta Geologica Academiae Scientiarum Hungaricae*, 24(1), 3–48.

Benton, M.J. (1986). More than one event in the late Triassic mass extinction. Nature, 321(6073), 857.Bernecker, M. (2005). Late Triassic reefs from the northwest and south Tethys: distribution, setting, and biotic composition. *Facies*, 51(1-4), 442-453.

Burgess, P.M. (2001). Modeling carbonate sequence development without relative sea-level oscillations. *Geology*, 29, 1127-1130.

Catuneanu, O., Galloway, W.E., Kendall, C.G.S.C., Miall, A.D., Posamentier, H.W., Strasser, A., & Tucker, M. E. (2011). Sequence stratigraphy: methodology and nomenclature. *Newsletters on Stratigraphy*, 44(3), 173-245.

Catuneanu, O., Abreu, V., Bhattacharya, J. P., Blum, M. D., Dalrymple, R. W., Eriksson, P. G., Fielding, C.R., Fisher, W.L., Galloway, W.E., Gibling, M.R., & Giles, K. A. (2009). Towards the standardization of sequence stratigraphy. *Earth-Science Reviews*, *92*(1-2), 1-33.

Colombié, C., & Strasser, A. (2003). Depositional sequences in the Kimmeridgian of the Vocontian Basin (France) controlled by carbonate export from shallow-water platforms. *Geobios*, *36*(6), 675-683.

Czurda, K., & Nicklas, L. (1970). Zur Mikrofazies und Mikrostratigraphie des Hauptdolomites und Plattenkalk-Niveaus der Klostertaler Alpen und des Rhätikon. *Festbandd. Geol. Inst. 300-Jahr-Feier Univ*. Innsbruck, 165-253.

Deenen, M.H., Ruhl, M., Bonis, N.R., Krijgsman, W., Kuerschner, W.M., Reitsma, M., & Van Bergen, M.J. (2010). A new chronology for the end-Triassic mass extinction. *Earth and Planetary Science Letters*, *291*(1-4), 113-125.

Detre, C.S., Dosztály, L., & Herman, V. (1986). Uj kicsavarodott Ammonoidea-lelet a hazai triászból. *Asványgyüjtö Figyelö* 3: 24 - 27.

Embry, J.C., Vennin, E., Van Buchem, F.S.P., Schroeder, R., Pierre, C., & Aurell, M. (2010). Sequence stratigraphy and carbon isotope stratigraphy of an Aptian mixed carbonate-siliciclastic platform to basin transition (Galve sub-basin, NE Spain). *Geological Society, London, Special Publications*, *329*(1), 113-143.

Farouk, S., Thibault, N., Jaff, R.B.N., Faris, M., Ahmad, F., & Khashaba, A. (2018). An integrated study of upper Campanian-lower Maastrichtian carbon isotopes and calcareous plankton biostratigraphy of the Kurdistan Region, northeastern Iraq. *Cretaceous Research* 82, 64-80.

Fischer, A. G. (1964). The Lofer cyclothems of the Alpine Triassic. *Kansas State Geological Survey Bulletin* 169, 107-149.

Gawlick, H.J., & Böhm, F. (2000). Sequence and isotope stratigraphy of late triassic distal periplatform limestones from the northern calcareous alps (Kälberstein quarry, Berchtesgaden hallstatt zone). *International Journal of Earth Sciences*, 89, 108-129.

Gnaccolini, M. (1965). Calcare di Zu e Argilliti di Riva di Solto: due formazioni del Retico Lombardo. *Riv. Ital. Paleontol. Stratigr.* 71, 1099-1121.

Goldhammer, R.K., Dunn, P.A., & Hardie, L.A. (1990). Depositional cycles, composite sea-level changes, cycle stacking patterns, and the hierarchy of stratigraphic forcing: Examples from Alpine Triassic platform carbonates. *Geological Society of America Bulletin* 102, 535-562.

Golebiowski, R. (1989). *Stratigraphie und Biofazies der Kössener Formation (Obertrias, Nördliche Kalkalpen)*. Ph.D. dissertation. University of Vienna, Austria.

Golebiowski, R. (1990). The Alpine Kössen Formation, a key for european topmost Triassic correlations. *Albertiana*, 8, 25-35.

Golebiowski, R. (1991). Becken und Riffe der alpinen Obertrias: Lithostratigraphie und Biofazies der Kössener Schichten. – In: Nagel, D. & Rabeder, G. (Eds.): *Exkursionen im Jungpaläozoikum und Mesozoikum Österreichs*, 79-119, Wien (Österreichische Paläontologische Gesellschaft).

Guex, J., Bartolini, A., Atudorei, V., & Taylor, D. (2004). High-resolution ammonite and carbon isotope stratigraphy across the Triassic–Jurassic boundary at New York Canyon (Nevada). *Earth and Planetary Science Letters* 225, 29–41.

Haas, J., Kovács, S., Krystyn, L., & Lein, R. (1995). Significance of Late Permian-Triassic facies zones in terrane reconstructions in the Alpine-North Pannonian domain. *Tectonophysics*, *242*(1-2), 19-40.

Haas, J., Götz, A.E., & Pálfy, J. (2010a). Late Triassic to Early Jurassic palaeogeography and eustatic history in the NW Tethyan realm: new insights from sedimentary and organic facies of the Csővár Basin (Hungary). *Palaeogeography, Palaeoclimatology, Palaeoecology*, 291, 456-468.

Haas, J., Piros, O., Budai, T., & Görög, Á. (2010b). Transition Between the Massive Reef–Backreef and Cyclic Lagoon Facies of the Dachstein Limestone in the Southern Part of the Dachstein Plateau, Northern Calcareous Alps, Upper Austria and Styria. *Abhandlungen der Geologischen Bundesanstalt*, *65*, 35-56.

Hallam A., & Wignall P.B. (1997). Mass extinctions and their aftermath. Oxford University Press, Oxford, 320 p.

Hesselbo, S.P., Robinson, S.A., Surlyk, F., & Piasecki, S. (2002). Terrestrial and marine extinction at the Triassic-Jurassic boundary synchronized with major carbon-cycle perturbation: a link to initiation of massive volcanism? G*eology*, 30, 251-254.

Hillebrandt, A.V., Krystyn, L., Kürschner, W.M., Bonis, N.R., Ruhl, M., Richoz, S., Schobben, M.A.N., Urlichs, M., Bown, P.R., Kment, K., McRoberts, C.A., Simms, M., and Tomãsových, A. (2013). The global stratotype sections and point (GSSP) for the base of the Jurassic System at Kuhjoch (Karwendel Mountains, Northern Calcareous Alps, Tyrol, Austria). *Episodes*, *36*(3), 162-198.

Holstein, B. (2004). Palynologische Untersuchungen der Kössener Schichten (Rhät, Obertrias). *Jahrbuch der Geologischen Bundesanstalt* 144(3/4), 261–365.

Huck, S., Heimhofer, U., Rameil, N., Bodin, S., & Immenhauser, A. (2011). Strontium and carbon-isotope chronostratigraphy of Barremian–Aptian shoal-water carbonates: Northern Tethyan platform drowning predates OAE 1a. *Earth and Planetary Science Letters*, *304*(3-4), 547-558.

Huck, S., Heimhofer, U., Immenhauser, A., & Weissert, H. (2013). Carbon-isotope stratigraphy of Early Cretaceous (Urgonian) shoal-water deposits: Diachronous changes in carbonate-platform production in the north-western Tethys. *Sedimentary Geology* 290, 157-174.

Jadoul, F., Berra, F., & Frisia, S. (1992). Stratigraphic and paleogeographic evolution of a carbonate platform in an extensional tectonic regime: the example of the Dolomia Principale in Lombardy (Italy). *Riv. Ital. Paleontol. Stratigr.* 98, 29-44.

Jadoul, F., Galli, M.T., Muttoni, G., Rigo, M., & Cirilli, S. (2012). The late Norian-Hettangian stratigraphic and paleogeographic evolution of the Bergamasc Alps. In *Geological field trips* 4/1, 1-55. Istituto Superiore per la Protezione e la Ricerca Ambientale (ISPRA).

1058 Jarvis, I. A. N., Gale, A. S., Jenkyns, H. C., & Pearce, M. A. (2006). Secular variation in Late
1059 Cretaceous carbon isotopes: a new δ13C carbonate reference curve for the Cenomanian–
1060 Campanian (99.6–70.6 Ma). *Geological Magazine*, *143*(5), 561-608.
1061 Jenkyns, H.C. (1995). Carbon-isotope stratigraphy and paleoceanographic significance of the
1062 lower Cretaceous shallow-water carbonates of resolution Guyot, mid-pacific mountains. In
1063 *Proceedings of the ocean drilling program, scientific results*, 143, 99-104.
1064 Jenkyns, H.C., Jones, C.E., Gröcke, D.R., Hesselbo, S.P., & Parkinson, D.N. (2002).
1065 Chemostratigraphy of the Jurassic System: Applications, limitations and implications for
1066 paleoceanography. *Journal of the Geological Society* 159, 351-378.
1067 Kiessling, W., Aberhan, M., Brenneis, B., & Wagner, P.J. (2007). Extinction trajectories of
1068 benthic organisms across the Triassic–Jurassic boundary. *Palaeogeography,*
1069 *Palaeoclimatology, Palaeoecology* 244, 201–222.
1070 Korte, C., & Hesselbo, S.P. (2011). Shallow marine carbon and oxygen isotope and elemental
1071 records indicate icehouse–greenhouse cycles during the Early Jurassic. *Paleoceanography* 26,
1072 PA4219
1073 Korte, C., & Kozur, H.W. (2010). Carbon isotope stratigraphy across the Permian–Triassic
1074 boundary: A review. *Journal of Asian Earth Sciences* 39, 215–235.
1075 Korte, C., & Kozur, H.W. (2011). Bio- and chemostratigraphic assessment of carbon isotope
1076 records across the Triassic–Jurassic boundary at Csővár quarry (Hungary) and
1077 Kendlbachgraben (Austria) and implications for global correlations. *Bulletin of the Geological*
1078 *Society of Denmark* 59, 101–115.
1079 Korte, C., Kozur, H.W., Bruckschen, P., & Veizer, J. (2003). Strontium isotope evolution of Late
1080 Permian and Triassic seawater. *Geochimica et Cosmochimica Acta* 67, 47–62.
1081 Korte, C., Kozur, H.W., & Veizer, J. (2005). $\delta^{13}C$ and $\delta^{18}O$ values of Triassic brachiopods and
1082 carbonate rocks as proxies for coeval seawater and palaeotemperature. *Palaeogeography,*
1083 *Palaeoclimatology, Palaeoecology* 226, 287–306.
1084 Korte, C., Hesselbo, S.P., Jenkyns, H.C., Rickaby, R.E.M., & Spötl, C. (2009).
1085 Palaeoenvironmental significance of carbon- and oxygen-isotope stratigraphy of marine
1086 Triassic–Jurassic boundary sections in SW Britain. *Journal of the Geological Society, London*
1087 166, 431–445.
1088 Korte, C., Thibault, N., Ullmann, C. V., Clémence, M. E., Mette, W., Olsen, T. K., Rizzi, M., &
1089 Ruhl, M. (2017). Brachiopod biogeochemistry and isotope stratigraphy from the Rhaetian
1090 Eiberg section in Austria: potentials and limitations. *Neues Jahrbuch für Geologie und*
1091 *Paläontologie-Abhandlungen*, 284(2), 117-138.
1092 Korte, C., Ruhl, M., Pálfy, J., Ullmann, C.V., & Hesselbo, S.P. (2019). Chemostratigraphy
1093 across the Triassic–Jurassic boundary. In: Sial, A.N., Gaucher, C., Ramkumar, M., Ferreira,
1094 V.P. (Eds.): Chemostratigraphy Across Major Chronological Boundaries, *Geophysical*
1095 *Monograph* 240, 185–210. American Geophysical Union. John Wiley & Sons, Inc.
1096 Kozur H.W. (1997). Pelagic Permian and Triassic of the western Tethys and its paleogeographic
1097 and stratigraphic significance. XLVIII. Berg- und Hüttenmännischer Tag, Technische
1098 Universität Bergakademie Freiberg, Kolloquium 1 Stratigraphie, Sedimentation und
1099 Beckenentwicklung im Karbon und Perm, 21–25.
1100 Kozur, H., & Mock, R. (1991). New Middle Carnian and Rhaetian conodonts from Hungary and
1101 the Alps. Stratigraphic importance and tectonic implications for the Buda Mountains and
1102 adjacent areas. *Jahrbuch der Geologischen Bundesanstalt*, 134(2), 271–297.
1103 Krystyn, L. (1980). Stratigraphy of the Hallstatt region. – In: Schönlaub, H. (Ed.): Second
1104 European Conodont Symposium, Guidebook, Fieldtrip B: Triassic conodont localities of the
1105 Salzkammergut region. *Abhandlungen der Geologischen Bundesanstalt Wien*, 35, 69-98.

1106 Krystyn, L. (1987). Zur Rhät-Stratigraphie der Zlambach-Schichten (vorläufiger Bericht).
1107 *Sitzungsberichte der österreichischen Akademie der Wissenschaft der mathematisch-*
1108 *naturwissenschaftlichen Klasse, Abt. I*, 196: 21 - 36.
1109 Krystyn, L. (2008). An ammonoid-calibrated Tethyan conodont time scale of the late Upper
1110 Triassic. *Berichte der Geologischen Bundesanstalt* 76, 9-11.
1111 Krystyn, L. (2010). Decision report on the defining event for the base of the Rhaetian stage:
1112 *Albertiana* 38, 11-12.
1113 Krystyn L., Böhm F., Kürschner W., & Delecat S. (2005). The Triassic –Jurassic boundary in the
1114 Northern Calcareous Alps. In: Pálfy, J. and Ozsvárt, P. (Eds.): Program, abstracts and field
1115 guide. *5th field workshop of IGCP 458 project* (Tata and Hallein, September 2005).
1116 Krystyn, L., Bouquerel, H., Kuerschner, W.M., Richoz, S., & Gallet, Y. (2007). Proposal for a
1117 candidate GSSP for the base of the Rhaetian stage. In: Lucas, S.G. & Spielmann, J.A., (Eds.):
1118 The Global Triassic. *New Mexico Museum of Natural History and Science Bulletin* 41, 189-
1119 199.
1120 Krystyn L., Mandl, G.W., & Schauer, M. (2009). Growth and termination of the Upper Triassic
1121 platform margin of the Dachstein area (Northern Calcareous Alps, Austria). *Austrian Journal*
1122 *of Earth Sciences* 102, 23-33.
1123 Kuss, J. (1983). Faziesentwicklung in proximalen Intraplattform-Becken: Sedimentation,
1124 Palökologie und Geochemie der Kössener Schichten (Ober-Trias, Nördliche Kalkalpen).
1125 *Facies*, *9*(1), 61.
1126 Kürschner, W.M., Bonis, N.R., & Krystyn, L. (2007). Carbon-isotope stratigraphy and
1127 palynostratigraphy of the Triassic–Jurassic transition in the Tiefengraben section—Northern
1128 Calcareous Alps (Austria). *Palaeogeography, Palaeoclimatology, Palaeoecology* 244, 257-
1129 280.
1130 Lakew, T. (1990). Microfacies and cyclic sedimentation of the Upper Triassic (Rhaetian) Zu
1131 Limestone (Southern Alps). *Facies* 22, 187-232.
1132 Lindström, S., van de Schootbrugge, B., Hansen, K.H., Pedersen, G.K., Alsen, P., Thibault, N.,
1133 Dybkjær K., Bjerrum C.J. & Nielsen, L.H. (2017). A new correlation of Triassic–Jurassic
1134 boundary successions in NW Europe, Nevada and Peru, and the Central Atlantic Magmatic
1135 Province: A time-line for the end-Triassic mass extinction. *Palaeogeography,*
1136 *Palaeoclimatology, Palaeoecology*, 478, 80-102.
1137 Mandl, G.W. (1999). The Alpine sector of the Tethyan shelf—examples of Triassic to Jurassic
1138 sedimentation and deformation from the Northern Calcareous Alps. *Mitteilungen der*
1139 *Österreichischen Geologischen Gesellschaft*, 92, 61-77.
1140 Maron, M., Rigo, M., Bertinelli, A., Katz, M. E., Godfrey, L., Zaffani, M., & Muttoni, G. (2015).
1141 Magnetostratigraphy, biostratigraphy, and chemostratigraphy of the Pignola-Abriola section:
1142 New constraints for the Norian-Rhaetian boundary. *Bulletin*, *127*(7-8), 962-974.
1143 Marshall, J.D. (1992). Climatic and oceanographic isotopic signals from the carbonate rock
1144 record and their preservation. *Geological Magazine*, 129, 143-160.
1145 McArthur, J.M., Tyson, R.V., Thomson, J., & Mattey, D. (1992). Early diagenesis of marine
1146 organic matter: Alteration of the carbon isotopic composition. *Marine Geology*, *105*(1-4), 51-
1147 61.
1148 McRoberts, C.A., Furrer, H., & Jones, D.S. (1997). Palaeoenvironmental interpretation of a
1149 Triassic-Jurassic boundary section from Western Austria based on palaeoecological and
1150 geochemical data. *Palaeogeography, Palaeoclimatology, Palaeoecology* 136, 79-95.
1151 Meschede, M. (2015). Die Entwicklung der Alpen. In: Meschede, M. (Ed.): Geologie
1152 Deutschlands, Springer, 161-174.

1153 Mette, W., Elsler, A., & Korte, C. (2011). Ostracods and $\delta^{18}O$ analysis in the Late Triassic of the
1154 Northern Calcareous Alps–implications for palaeotemperature and sea level fluctuations.
1155 *Joannea Geol. Paläont.* 11, 137-140.
1156 Mette, W., Elsler, A., & Korte, C. (2012). Palaeoenvironmental changes in the Late Triassic
1157 (Rhaetian) of the Northern Calcareous Alps: clues from stable isotopes and microfossils.
1158 *Palaeogeography, Palaeoclimatology, Palaeoecology* 350, 62-72.
1159 Mette, W., Thibault, N., Krystyn, L., Korte, C., Clémence, M.-E., Ruhl, M., Rizzi, M., &
1160 Ullmann, C.V. (2016): Rhaetian (Late Triassic) biotic and carbon isotope events and
1161 intraplatform basin development in the Northern Calcareous Alps, Tyrol, Austria. – *Geo.Alp*,
1162 13: 233-256.
1163 Mette, W., Clemence, M.E., Thibault, N., Korte, C., Konrad, B., & Ullmann, C.V. (2019).
1164 Sedimentology, carbon isotope stratigraphy and micropalaeontology of the Rhaetian
1165 Zlambach Formation–Implications for the Dachstein carbonate platform development
1166 (Northern Calcareous Alps, Austria). *Sedimentary Geology*, *382*, 47-60.
1167 Meyers, P.A. (1994). Preservation of elemental and isotopic source identification of sedimentary
1168 organic matter. *Chemical geology*, *114*(3-4), 289-302.
1169 Mitchell, S. F., Ball, J. D., Crowley, S. F., Marshall, J. D., Paul, C. R., Veltkamp, C. J., & Samir,
1170 A. (1997). Isotope data from Cretaceous chalks and foraminifera: Environmental or diagenetic
1171 signals? *Geology*, *25*(8), 691-694.
1172 Morante, R., & Hallam, A. (1996). Organic carbon isotopic record across the Triassic-Jurassic
1173 boundary in Austria and its bearing on the cause of the mass extinction. *Geology*, *24*(5), 391-
1174 394.
1175 Mostler, H., Scheuring, B., & Urlichs, M. (1978). Zur Mega-, Mikrofauna und Mikroflora der
1176 Kössener Schichten (alpine Obertrias) vom Weißloferbach in Tirol unter besonderer
1177 Berücksichtigung der in der *suessi*- und *marshi*-Zone auftretenden Conodonten.
1178 *Schriftenreihe der erdwissenschaftlichen Kommission der österreichischen Akademie der*
1179 *Wissenschaft* 4, 141-174.
1180 Muttoni, G., Mazza, M., Mosher, D., Katz, M. E., Kent, D. V., & Balini, M. (2014). A Middle–
1181 Late Triassic (Ladinian–Rhaetian) carbon and oxygen isotope record from the Tethyan Ocean.
1182 *Palaeogeography, Palaeoclimatology, Palaeoecology*, 399, 246-259.
1183 Pandolfi J.M. (2011) The Paleoecology of Coral Reefs. In: Dubinsky Z., Stambler N. (Eds.):
1184 Coral Reefs: An Ecosystem in Transition. Springer, Dordrecht, 13-24.
1185 Pálfy, J., Mortensen, J.K., Carter, E.S., Smith, P.L., Friedman, R.M., & Tipper, H.W. (2000).
1186 Timing of the end-Triassic mass extinction: First on land, then in the sea? *Geology* 28, 39-42.
1187 Pálfy, J., Demény, A., Haas, J., Hetényi, M., Orchard, M.J., & Vető, I. (2001): Carbon isotope
1188 anomaly and other geochemical changes at the Triassic-Jurassic boundary from a marine
1189 section in Hungary. *Geology* 29, 1047-1050.
1190 Pálfy, J. Demény, A., Haas, J., Carter, E.S., Görög, A., Halász, D. Oravecz-Scheffer, A.,
1191 Hetényi, M., Márton, E., Orchard, M.J., Ozsvárt, P., Vető, I., & Zajzon, N. (2007). Triassic–
1192 Jurassic boundary events inferred from integrated stratigraphy of the Csővár section,
1193 Hungary. *Palaeogeography, Palaeoclimatology, Palaeoecology* 244, 11-33.
1194 Preto, N., Agnini, C., Rigo, M., Sprovieri, M., & Westphal, H. (2013). The calcareous
1195 nannofossil Prinsiosphaera achieved rock-forming abundances in the latest Triassic of western
1196 Tethys: consequences for the δ 13 C of bulk carbonate. *Biogeosciences*, 10(9), 6053-6068.
1197 Reinhold, C., & Kaufmann, B. (2010). Sea-level changes as controlling factor of early
1198 diagenesis: the reefal limestones of Adnet (Late Triassic, Northern Calcareous Alps, Austria).
1199 *Facies*, *56*(2), 231-248.

1200 Richoz, S., Krystyn, L., Spötl, C., & Kürschner, W. (2008). Building an Upper Triassic carbon
1201 isotope reference curve. *Berichte Geol. Bundesanst.* 76, 17-19.
1202 Ruhl, M., & Kürschner, W.M., (2011). Multiple phases of carbon cycle disturbance from large
1203 igneous province formation at the Triassic–Jurassic transition. *Geology* 39, 431-434.
1204 Ruhl, M., Kürschner, W.M., & Krystyn, L. (2009). Triassic–Jurassic organic carbon isotope
1205 stratigraphy of key sections in the western Tethys realm (Austria). *Earth and Planetary*
1206 *Science Letters* 281, 169-187.
1207 Sackett, W.M., 1989. Stable carbon isotope studies on organic matter in the marine environment.
1208 In Fritz, P., and Fontes, J.C. (Eds.): Handbook of Environmental Isotope Geochemistry (Vol.
1209 3): The Marine Environment, 139−169. Elsevier, Amsterdam.
1210 Saltzman, M.R., Thomas, E., 2012. Carbon Isotope Stratigraphy. In: Gradstein et al. (Eds.): The
1211 Geologic Time Scale 2012. Elsevier, pp. 207–232.
1212 Satterley, A.K., & Brandner, R. (1995). The genesis of Lofer cycles of the Dachstein Limestone,
1213 Northern Calcareous Alps, Austria. *Geologische Rundschau* 84, 287-292.
1214 Satterley, A.K. (1996). The interpretation of cyclic successions of the Middle and Upper Triassic
1215 of the Northern and Southern Alps. *Earth-Science Reviews* 40, 181-207.
1216 Schäfer, P. (1979). Fazielle Entwicklung und palökologische Zonierung zweier Obertriadischer
1217 Riffstrukturen in den Nördlichen Kalkalpen ("Oberrhät" Riff-Kalke, Salzburg). *Facies* 1(1),
1218 3-245.
1219 Schlager, W. (2004). Fractal nature of stratigraphic sequences. *Geology* 32, 185-188.
1220 Schlager, W. (2005). Carbonate Sedimentology and Sequence Stratigraphy, Concepts in
1221 Sedimentology and Paleontology #8, Society of Economic Paleontologists and Mineralogists
1222 (SEPM), 200 p.
1223 Schlager, W., Reijmer, J. J. G., Droxler, A. (1994). Highstand shedding of carbonate platforms.
1224 *Journal of Sedimentary Research* 64, 270-281.
1225 Somma R., Martin-Rojas I., Zamparelli V., Estévez A., & Perrone V. (2010) First record of
1226 Tethyan Ladinian foraminifer-rich beds in the Betic Internal Zone (SE Spain). *Geogaceta* 48,
1227 67-70.
1228 Strasser, A., Pittet, B., Hillgärtner, H., & Pasquier, J. B. (1999). Depositional sequences in
1229 shallow carbonate-dominated sedimentary systems: concepts for a high-resolution analysis.
1230 *Sedimentary Geology*, *128*(3-4), 201-221.
1231 Suess, E. (1852). Untersuchungen der Brachiopoden in den sogenannten Kalkschichten von
1232 Kössen. *Jahrbuch der Geologischen Reichsanstalt*, 3(1): 180-181.
1233 Tanner, L. H. (2010). The Triassic isotope record. *Geological Society, London, Special*
1234 *Publications*, *334*(1), 103-118.
1235 Tanner, L.H., Lucas, S. G., & Chapman, M. G. (2004). Assessing the record and causes of Late
1236 Triassic extinctions. *Earth-Science Reviews*, 65(1-2), 103-139
1237 Tomašových, A. (2006a). Brachiopod and bivalve ecology in Late Triassic (Alps, Austria):
1238 onshore-offshore replacements caused by variations in sediment and nutrient supply. *Palaios*
1239 21, 344-368.
1240 Tomašových, A. (2006b). Linking taphonomy to community-level abundance: insights into
1241 compositional fidelity of the Upper Triassic shell concentrations (Eastern Alps).
1242 *Palaeogeography, Palaeoclimatology, Palaeoecology* 235, 355-381.
1243 Ullmann, C.V., & Korte, C. (2015). Diagenetic alteration in low-Mg calcite from macrofossils:
1244 A review. *Geological Quarterly*, 59 (1), 3-20.
1245 Ullmann, C.V., Campbell, H.J., Frei, R., Hesselbo, S.P., Pogge von Strandmann, P.A.E., &
1246 Korte, C. (2013). Partial diagenetic overprint of Late Jurassic belemnites from New Zealand:

Implications for the preservation potential of δ^7Li values in calcite fossils. *Geochimica et Cosmochimica Acta* 120, 80-96.

Ullmann, C.V., Campbell, H.J., Frei, R., & Korte, C. (2014). Geochemical signatures in Late Triassic brachiopods from New Caledonia. *New Zealand Journal of Geology and Geophysics* 57 (4), 420-431.

Urlichs, M. (1972). Ostracoden aus den Kössener Schichten und ihre Abhängkeit von der Ökologie. *Mitteilungen der Gesellschaft der Geologie- und Bergbaustudenten in Österreich* 21, 661-710.

Veizer, J. (1983). Chemical diagenesis of carbonates: Theory and application of trace element technique. – In: Arthur, M.A., *et al*. (Eds.): Stable Isotopes in Sedimentary Geology, Society of Economic Palaeontologists and Mineralogists Short Course, 10: 3/1-3/100, Tulsa.

Veizer, J., Ala, D., Azmy, K., Bruckschen, P., Buhl, D., Bruhn, F., Carden, G.A.F., Diener, A., Ebneth, S., Goddéris, Y., Jasper, T., Korte, C., Pawellek, F., Podlaha, O.G. & Strauss, H. (1999). ^{87}Sr/^{86}Sr, δ^{13}C and δ^{18}O evolution of Phanerozoic seawater. *Chemical Geology* 161, 59-88.

von Buch, L. (1828). Über die Kalke mit Gervillia u. Avicula. – *Abhandlungen der Berliner Akademie*.

Ward, P.D., Garrison, G.H., Williford, K.H., Kring, D.A., Goodwin, D., Beattie, M.J., & McRoberts, C.A. (2007): The organic carbon isotopic and paleontological record across the Triassic–Jurassic boundary at the candidate GSSP section at Ferguson Hill, Muller Canyon, Nevada, USA. *Palaeogeography, Palaeoclimatology, Palaeoecology* 244, 281-289.

Williford, K.H., Ward, P.D., Garrison, G.H., & Buick, R., (2007). An extended organic carbon-isotope record across the Triassic–Jurassic boundary in the Queen Charlotte Islands, British Columbia, Canada. *Palaeogeography, Palaeoclimatology, Palaeoecology* 244, 290-296.

Whiteside, J.H., & Ward, P.D. (2011). Ammonoid diversity and disparity track episodes of chaotic carbon cycling during the early Mesozoic. *Geology* 39, 99-102.

Zaffani, M., Agnini, C., Concheri, G., Godfrey, L., Katz, M., Maron, M., & Rigo, M. (2017). The Norian "chaotic carbon interval": New clues from the δ13Corg record of the Lagonegro Basin (southern Italy). *Geosphere*, *13*(4), 1133-1148.

Zaffani, M., Jadoul, F., & Rigo, M. (2018). A new Rhaetian $\delta^{13}C_{org}$ record: Carbon cycle disturbances, volcanism, End-Triassic mass Extinction (ETE). *Earth-Science Reviews* 178, 92-104.

This is the author-formatted final version of Rizzi et al. (2020), Global and Planetary Change, accepted May 4th 2020, article 103210 https://doi.org/10.1016/j.gloplacha.2020.103210

1279 **Supplementary material**

1280 Appendix A: Original description of microfacies of the Eiberg Basin by Golebiowski (1989)

1281 Table S1: Bulk carbonate carbon and oxygen isotopes ($\delta^{13}C$ and $\delta^{18}O$)

1282 Table S2: Bulk organic carbon isotopes ($\delta^{13}C_{org}$)

1283 Table S3: Total organic carbon values (TOC) and carbonate content (%$CaCO_3$)

1284 Table S4: Brachiopod carbon and oxygen isotopes ($\delta^{13}C$ and $\delta^{18}O$)

1285 Table S5: Carbon and oxygen isotopes of calcite veins ($\delta^{13}C$ and $\delta^{18}O$)

1286